EUROPEAN ORGANIZATION FOR NUCLEAR RESEARCH
CERN - AB DEPARTMENT

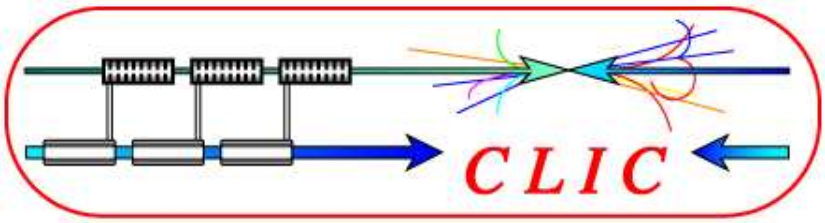

CLIC-Note-764

CLIC 2008 PARAMETERS

H. Braun, R. Corsini, J.-P. Delahaye, A. De Roeck, S. Doebert, G. Geschonke, A. Grudiev, C. Hauviller, B. Jeanneret, E. Jensen, T. Lefevre, Y. Papaphilippou, G. Riddone, L. Rinolfi, W.-D. Schlatter, H. Schmickler, D. Schulte, I. Syratchev, M. Taborelli, F. Tecker (editor), R. Tomás, S. Weisz, W. Wunsch,
CERN, Geneva,
A. Ferrari, Uppsala University,

for the CLIC study team

Abstract

This note presents the CLIC parameter set as of beginning 2008 and describes the different sub-systems, pointing out how the design of the different components is driven.
This design emerged from an updated understanding of limitations for normal conducting accelerating structures, which led to a new optimised design for the CLIC 12 GHz accelerating structure. The structure parameters and improvements in other sub-systems have resulted in a major revision of the parameters. The overall layout and efficiencies for CLIC with this updated parameter-set are presented.

Geneva, Switzerland
October 2, 2008

Contents

1 Overview and Rationale

The last CLIC parameter revision before this one was completed in 2005 [1]. In the 2005 revision two key numbers, namely the frequency of 30 GHz and the gradient of 150 MV/m were treated as fixed input specifications rather than as parameters for optimization. However, already then it was realized that further studies have to be undertaken to validate or refute this choice of key parameters. Shortly after the 2005 revision, new experimental results from RF structure testing in the test facilities CTF3 and NLCTA indicated that

- The very promising results obtained in CTFII with 30 GHz Molybdenum iris structures tested at short pulse-length cannot be extrapolated to a pulse length as required for high luminosity operation of CLIC.
- The RF criteria for structure design needed refinement, taking into account the observation that not only total power flow but also power flow density is constraining structure performance.
- The RF breakdown probability of accelerating structures permissible for operation imposes another important constraint, limiting design gradients further. With this constraint the anticipated gain from refractive metals instead of copper as structure material virtually vanished.

The new data practically excluded 150 MV/m as a reasonable design goal with the structure technologies at hand. Earlier experiments had already shown that the trend of increasing accelerating gradient with RF frequency observed in the regime below 3 GHz is not maintained at high frequencies. It was in fact found that in the frequency range 12 GHz - 30 GHz the maximum achievable acceleration has no significant dependence on frequency at given RF pulse length.

With all this in mind, a systematic scan of accelerating structure parameters and related beam parameters was started in 2006 making maximum use of available experimental data from CTF3 and NLC/JLC to define the best RF frequency and gradient. In addition to the luminosity over grid power figure of merit used for the 2005 parameter optimisation a scalable cost model was introduced to understand the cost impact of the parameter choice.

This optimisation revealed an optimum acceleration field of 100 MV/m as the best trade off between performance and cost for a rather flat frequency optimum around 14 GHz. In order to be able to test structures with the new frequency in the CLIC test facility CTF3, the frequency choice was further constrained to integer multiples of 2.99855 GHz.

With all this input, the remaining frequency choices were 11.9942 GHz and 14.9928 GHz. In order to profit from the substantial know-how and hardware investment available for X-band from the discontinued NLC and JLC studies it was decided to choose the lower value of 11.9942 GHz, which is closer to the NLC/JLC frequency of 11.4 GHz in order to build on the successful R&D done in the past by the NLC and JLC studies and to take advantage of the large expertise and test facilities available at this frequency. For the choice of the beam parameters more emphasize was put on technical margins and feasibility, in order to assure a credible conceptual design for 2010.

Following these key choices all other subsystem parameters were reviewed and modified for consistency. This exercise followed very much the same strategy as already taken and described in the 2005 parameter note.

After a reminder of the major Physics requirements in the next section, this note briefly describes the design procedure and main parameters of the various sub-systems of the CLIC complex at the nominal beam collision energy of 3 TeV. The major parameters are summarized in Appendix A.

2 Physics Requirements

The next energy frontier in High Energy Physics is the TeV energy range, and will first be explored by the LHC which will come on-line at the end of 2008. The data of this collider are eagerly awaited for and will set the scene for the high energy frontier in particle physics for the next decade and more. Just as e^+e^- colliders provided an essential complement to hadron–hadron colliders in the 100 GeV energy range, establishing beyond doubt the validity of the Standard Model, so we expect that higher-energy e^+e^- colliders will be needed to help unravel the TeV physics, to be unveiled by the LHC. They provide very clean experimental environments and democratic production of all particles within the accessible energy range, including those with only electroweak interactions. These considerations motivate several projects for e^+e^- future colliders. The collider considered in this report has the so far unique feature that it aims for an e^+e^- centre of mass energy of 3 TeV and possibly higher, at high luminosities.

The best candidate for new physics at the TeV scale is that associated with generating masses for elementary particles. This is expected to involve a Higgs boson, or something to replace it. The precision electroweak data from LEP and elsewhere rule out many alternatives to the single elementary Higgs boson predicted by the Standard Model, and suggest that it should weigh $\lesssim 200$ GeV. A single elementary Higgs boson is not thought to be sufficient by itself to explain the variety of the different mass scales in physics. Many theories beyond the Standard Model, such as those postulating supersymmetry, extra dimensions or new strong interactions, predict the appearance of non-trivial new dynamics at the TeV scale.

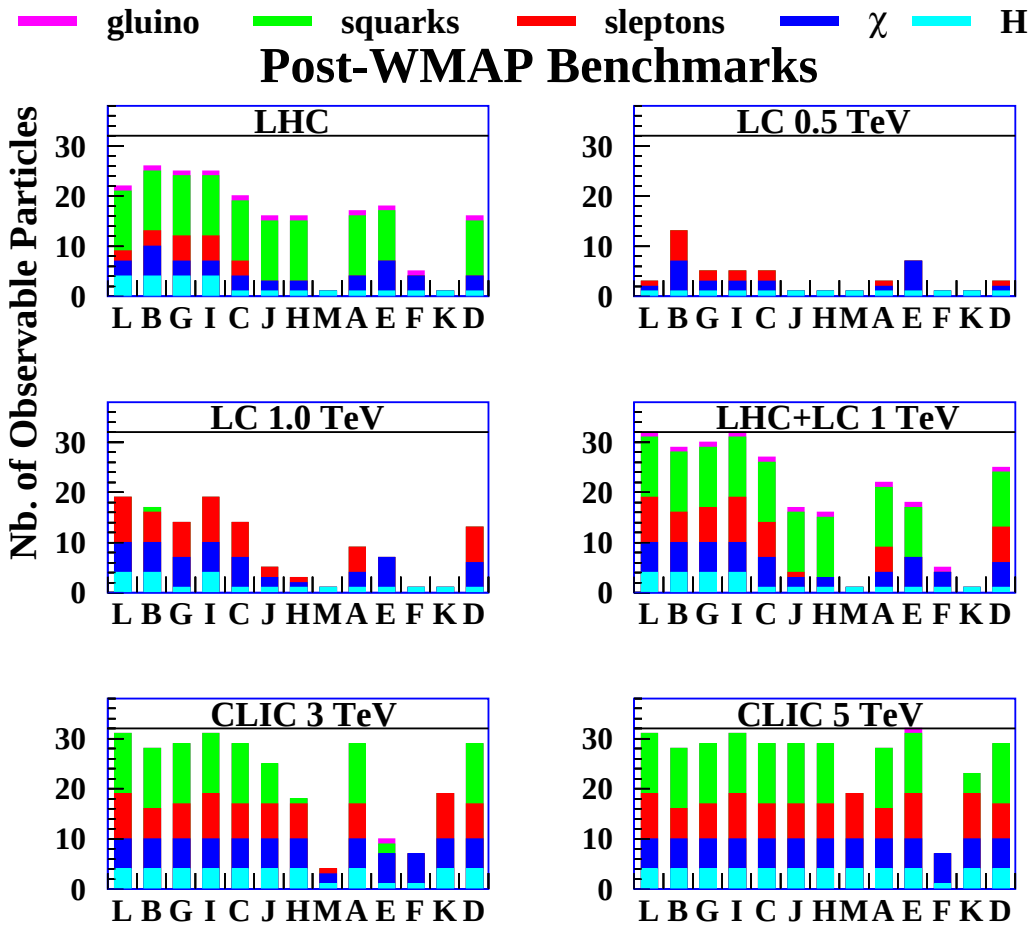

Figure 1: Bar charts of the numbers of different sparticle species observable in a number of benchmark supersymmetric scenarios at different colliders, including the LHC and linear e^+e^- colliders with various centre-of-mass energies. The benchmark scenarios are ordered by their consistency with the most recent BNL measurement of $g_\mu - 2$ and are compatible with the WMAP data on cold dark matter density. We see that there are some scenarios where the LHC discovers only the lightest neutral supersymmetric Higgs boson. Lower-energy linear e^+e^- colliders largely complement the LHC by discovering or measuring better the lighter electroweakly-interacting sparticles. Detailed measurements of the squarks would, in many cases, be possible only at CLIC.

For example, supersymmetry predicts that every particle in the Standard Model should be accompanied by a supersymmetric partner weighing $\lesssim 1$ TeV. Alternatively, theories with extra spatial dimensions predict the appearance of new particle excitations or other structural phenomena at the TeV scale. Finally, alternatives to an elementary Higgs boson, such as new strong interactions, also predict many composite resonances and other effects observable at the TeV energy scale.

Whilst there is no direct evidence, there are various indirect experimental hints that there is indeed new dynamics at the TeV scale. One is the above-mentioned agreement of precision electroweak data with the Standard Model, *if* there is a relatively light Higgs boson. Another is the agreement of the gauge couplings measured at LEP and elsewhere with the predictions of simple grand unified theories, *if* there is a threshold for new physics at the TeV scale, such as supersymmetry. Another hint may be provided by the apparent dominance of dark matter in the Universe, which may well consist of massive, weakly-interacting particles, *in which case* they should weigh $\lesssim 1$ TeV.

We expect that the clean experimental conditions at a linear e^+e^- collider will enable many detailed measurements of this new dynamics to be made. If there is a light Higgs boson, its properties will have been studied at the LHC and an e^+e^- collider with CMS energy up to one TeV, such as proposed by the ILC project, but one would wish to

verify the mechanism of electroweak symmetry breaking (EWSB) by measuring the Higgs self-coupling associated with its effective potential, which would be done better at a higher-energy e^+e^- collider. Furthermore if the Higgs boson is relatively heavy, measurements of its properties at the LHC or a lower-energy TeV scale e^+e^- collider will quite possibly have been incomplete. As another example, if Nature has chosen supersymmetry, it is quite likely that the LHC and a TeV-scale e^+e^- collider will not have observed the complete sparticle spectrum, as seen in Fig. 1.

Moreover, in many cases detailed measurements at a multi-TeV e^+e^- collider would be needed to complement previous exploratory observations, e.g. of squark masses and mixing, or of heavier charginos and neutralinos. Analogous examples of the possible incompleteness of measurements at the LHC collider can be given in other scenarios for new physics, such as extra dimensions. A Multi-TeV collider will increase the sensitivity range of the LHC by a factor five or more. Even if extra dimensions are discovered before, it would, for example, be fascinating to study in detail at CLIC a Kaluza–Klein excitation of the Z boson that might have been discovered at the LHC. In recent years many new ideas and models have been discussed which lead to new particles produced with masses in the TeV range, such as Little Higgs models, Hidden Valley physics and others.

Other examples of increased physics reach relative to the LHC are

- Z' production: the increase in sensitivity to Z' is about a factor 5 larger at a multi-TeV collider.
- Compositness: the sensitivity to the compositness scale can be increased by a factor 10.
- The sensitivity to triple gauge boson couplings is increased by a factor 10.

Moreover, in case the EWSB is not driven by the Higgs, new phenomena in WW scattering at the TeV scale can be discovered at the LHC but are often difficult to study in detail, while at a multi-TeV collider this region can be probed with very high precision and e.g. new resonances can be measured with high accuracy.

A detailed study of the physics potential of CLIC, including a close integration of experiments at linear e^+e^- colliders with the accelerator, particularly in the final-focus region, has been performed in [2], using preliminary sets of machine parameters. It was demonstrated that, when taking into account a realistic luminosity spectrum and realistic background conditions, precision measurements can be made at a multi-TeV collider. It is important that a high total luminosity is kept since the cross sections of s-channel processes scale as $1/s$ ($s = E^2_{\mathrm{CMS}}$). On the other hand t-channel production rises as $\ln(s)$ and these cross sections get larger than the s-channel ones in the multi-TeV domain. The precise control of the luminosity spectrum will be important for precision measurements. For resonance scans, performed by varying the CMS energy of the machine, narrow, somewhat reduced luminosity spectra yield about the same final precision as the full broader luminosity spectra. But for measurements such as the Higgs self-coupling the total luminosity is most important. Hence to keep the total luminosity as high as possible is an important requirement for the machine

Since CLIC operates in the high beamstrahlungs regime, the background of e^+e^- pairs and hadronic $\gamma\gamma$ interactions is large. This imposes strong requirements on the detector design. With the assumed background numbers based on earlier preliminary parameter sets, the precision is not compromised significantly, but a reduction in background at the interaction point would be certainly beneficial.

The short time between bunches is also a challenge for the detectors. The even shorter bunch crossing time as foreseen by the new parameters for CLIC will make this challenge harder, but is not expected to be preventive for producing high precision measurements. The detectors will however not be fast enough to time-stamp individual bunch crossings but one will need to integrate over a bunch train or a large part of it, which means that the backgrounds of several, perhaps as many as 20, bunch crossings will be accumulated. The resulting large number of overlap events is reminiscent of the experimental conditions at the LHC. However the situations here is somewhat different: most of the background activity from $\gamma\gamma$ collisions will be interactions at low CMS energy and therefore will not affect the hard scattering signatures.

The higher CMS energy of CLIC also leads to more collimated high energy objects such as jets in the detector. Energy flow measurements may be less effective than for detectors at a collider up to 1 TeV CMS energy. The calorimeter choice for a detector at CLIC may need some further study.

In view of the detector and detector machine interface challenges mentioned above, a detector R&D program is being put in place in close collaboration with the ILC detector efforts. The background predictions for CLIC and its machine parameters as discussed in this document will be used in these studies.

In all, the final parameters of CLIC will have a notable influence on the final physics output and particularly on detector design choices, but precision physics will be possible, and the physics/discovery reach will remain large if the total luminosity remains larger than about $5 \cdot 10^{34}$ cm^{-2}s^{-1} as it is the case for the new parameter set.

3 Main Linac Accelerating Structures

3.1 Design of the accelerating structures

As stated in section 1, the new design of the main beam accelerating structure is a main driver for many of the parameters in this new set. The design is based on the idea of use of four waveguides to suppress the long-range transverse wakefields [3]. The geometry of the present Waveguide Damped Structure (WDS) cell is shown in Fig. 2.

The outer walls of the cell have elliptical shape which provide homogeneous distribution of the surface magnetic field. This reduces pulsed surface heating, due to a lower maximum current density. The corresponding surface magnetic and electric field distributions are shown in Fig. 3.

3.2 The Optimisation Procedure

The new structure optimisation procedure was motivated by the need to simultaneously vary iris diameter, iris thickness, RF phase advance per cell, RF frequency and average loaded accelerating gradient while considering the effect on short-range transverse wakefield amplitude, long-range transverse wakefield suppression, RF-to-beam efficiency, surface fields and power flow. The simple approach of varying a single parameter at a time was clearly impractical.

The optimisation procedure, which is repeated for different phase advances, consists of three parts for each fixed RF phase advance, RF frequency, and average loaded accelerating gradient. In the first part, a set of nine individually optimised cell geometries are calculated for fundamental-mode and lowest-dipole-mode characteristics for three different apertures *a*, and three different iris thicknesses *d*. This gives a two-dimensional parameter space for interpolation.

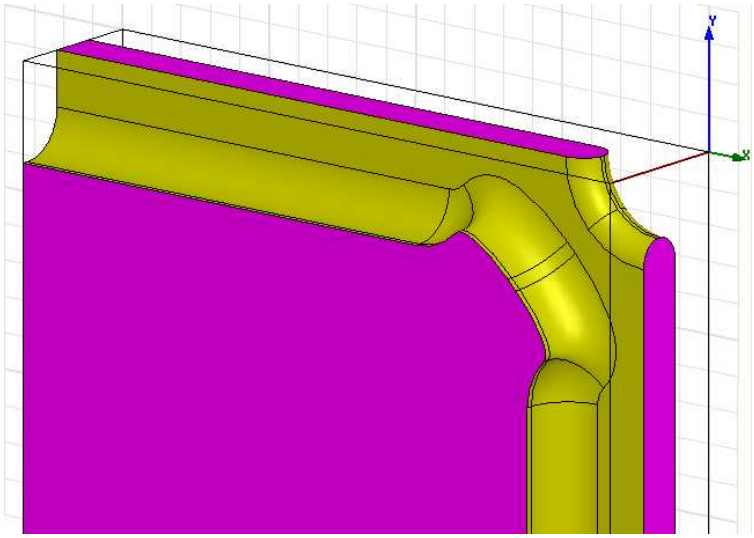

Figure 2: Geometry of the WDS cell. One quarter of a cells is shown to better demonstrate shape of the cell cavity and damping waveguides.

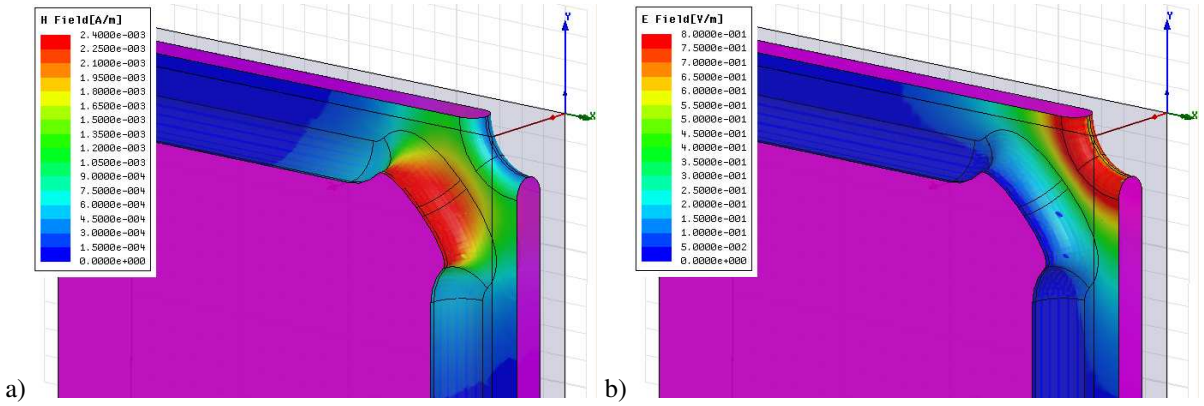

Figure 3: Surface magnetic (a) and electric (b) field distribution in WDS cell.

In the second part, parameters for $4 \cdot n_{d1} \cdot n_{d2} \cdot (n_{a1}-1) \cdot (n_{a2}-1)/2$ structures are calculated. Here n_{d1},n_{d2},n_{a1},n_{a2} mean number of variation in d_1, d_2, a_1, a_2, respectively, which are d and a in the first and last cells of a structure. For each structure the bunch charge N is determined from the results of beam dynamic simulations which take into account the effect of short-range wakefields on emittance growth [4]. The long-range wakefields of the lowest dipole mode are calculated based on interpolated parameters and an uncoupled model. The value of the transverse wake envelope at the position of the second bunch $||w(N_s\lambda_{\mathrm{RF}})||$ is limited by the following condition [4]:

$$N \cdot ||w(N_s\lambda_{\mathrm{RF}})||/E_a < 4 \cdot 10^9 \times 10\ \mathrm{kV/pCm^2}/150 MV/m \tag{1}$$

Satisfying this condition gives the bunch separation in the number of RF cycles N_s.

In the third part of the optimisation, structures are selected which satisfy the following RF constraints:

1. Surface electric field [5]: $E_{\mathrm{surf}}^{\mathrm{max}} < 260$ MV/m.
2. Pulsed surface heating [6]: $\Delta T^{\mathrm{max}} < 56$ K.
3. Power [7]: $P_{\mathrm{in}}/C\,{\tau_p}^{1/3} < 18\ \mathrm{MW/mm\,ns^{1/3}}$.

Here $E_{\mathrm{surf}}^{\mathrm{max}}$ and ΔT^{max} refer to maximum surface electric field and maximum pulsed surface heating temperature rise in the structure, respectively. P_{in}, C and τ_p denote input power, input iris circumference and pulse length, respectively. Since both $\Delta T^{\mathrm{max}} \propto \sqrt{\tau_p}$ and $P_{\mathrm{in}}/C\,{\tau_p}^{1/3}$ depend on pulse length conditions, 2 and 3 can always be satisfied by reducing the number of bunches N_b in the train. This reduction is however limited because the shorter the pulse the lower the RF-to-beam efficiency due to the fill time of the structure. Hence, N_b is chosen to make the pulse as long as possible under pulsed surface heating and power constraints. Then, if the structure satisfies condition (1), RF-to-beam efficiency and other pulse length dependent parameters of the structure are scaled for this value of N_b.

Though a different choice of optimisation criteria is possible, our main goal is to reach the design luminosity at a given energy in the most efficient way. Hence the optimum structure must provide the highest ratio of luminosity to main linac input power. In terms of the structure parameters this corresponds to maximizing the figure of merit: $L_{b\times}\eta/N$, where $L_{b\times}$ denotes the luminosity per bunch crossing in a 1% energy bin – this is obtained from beam dynamics simulations of the CLIC main linac and beam delivery system [4]. Thus, the optimum structure is that which gives the maximum of figure of merit for all structures satisfying conditions 1 through 3. In addition, a parameterized cost model [8] has been also used as optimization criteria.

It has to be noted that this optimisation procedure is based on a number of assumptions that are the best knowledge as of mid 2007. In the future, these assumptions may well change when new data becomes available. The RF power constraint [7] is the most uncertain number. It is based on 30 GHz and X-band data for copper structure. The two other RF constraints, pulsed surface heating and surface electric field, are also not known with any certainty. Finally, since breakdown behaviour is theoretically not well understood, there is no guarantee that there are no other RF constraints.

The optimisation procedure has been performed for a range of RF frequencies from 10 GHz to 30 GHz and for a range of average loaded accelerating gradients from 90 MV/m to 150 MV/m. The average iris radius to wave length ratio $<a>/\lambda$ was varied from 0.9 to 0.21, the iris thickness to wavelength ratio d/λ was varied from 0.025 to 0.1. A total number of structures anylized in the optimization procedure was 68 866 560. The total cost minimization results are presented in Fig. 4 and Fig. 5. Fig. 4 clearly indicates that the optimum RF frequency of CLIC main linac is not 30 GHz but rather X-band both from the point of view maximizing the FoM [see Fig. 4 a)] and minimizing the total cost [see Fig. 4 b)] . The optimum gradient is different depending on what is used as the optimization criterion. It is below 90 MV/m, the lowest gradient considered, if FoM is used and it is near 120 MV/m if total cost is used. A compromise has been found near 100 MV/m in order to profit from both lower cost and higher performance of CLIC.

A list of the parameters for the optimum structure (so-called CLIC_G), which are finally calculated without interpolation, is presented in Table 1. Fundamental mode parameters as a function of cell number are shown in Fig. 6 and the transverse wake is shown in Fig. 7.

As the optimum bunch charge for this structure is higher than in the previous parameter set, the injector complex and the damping ring design had to be updated to the new parameters.

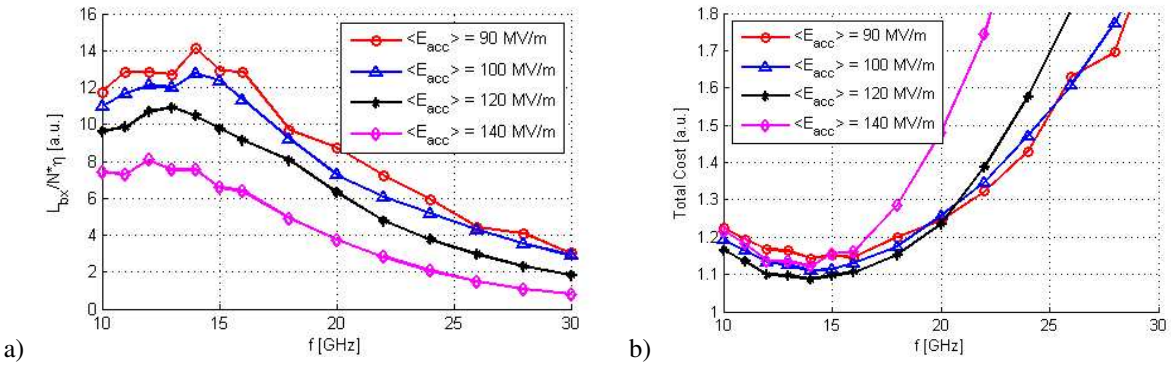

a) b)

Figure 4: Luminosity per power figure of merit (a) and total cost (b) as a function of RF frequency.

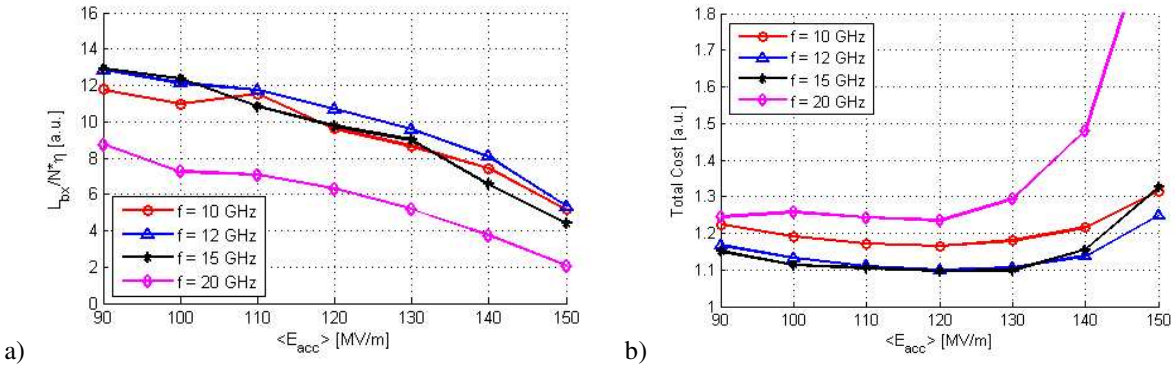

a) b)

Figure 5: Luminosity per power figure of merit (a) and total cost (b) as a function of average accelerating gradient.

$< E_{\rm acc} >$ [MV/m]	100
f [GHz]	11.994
RF phase advance per cell: $\Delta\phi$ [°]	120
Cell length: l_c [mm]	8.333
First and last iris radius: a_1, a_2 [mm]	3.15, 2.35
First and last iris thickness: d_1, d_2 [mm]	1.67, 1.00
First and last cell Q-factor: $Q_{1,2}$	6100, 6265
First and last cell shunt impedance $r_{1,2}$ [(Linac)MΩ/m]	89, 112
First and last cell group velocity: $v_g/c_{1,2}$ [%]	1.66, 0.83
Averaged a to wavelength ratio: $<a>/\lambda$	0.11
Number of particles in the bunch: N	3.72×10^9
Luminosity per bunch crossing: $L_{b\times}$ [m^{-2}]	1.22×10^{34}
$N_{\rm cell}$	24
Structure length (active): l [mm]	229
Bunch separation: N_s [RF cycles]	6
Number of bunches in the train: N_b	312
Pulse length: τ_p [ns]	240.8
Input power: P_{in} [MW]	63.8
RF-to-beam efficiency: η [%]	27.7

Table 1: Parameters of the best structure (so-called CLIC_G) calculated without interpolation.

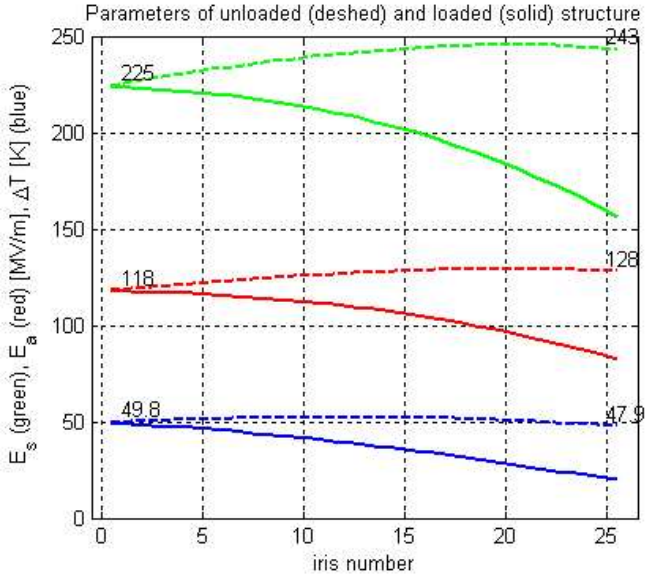

Figure 6: Pulsed surface heating temperature rise (blue), accelerating gradient (red), and maximum surface electric field (green) along the optimum structure with (solid) and without (dashed) beam loading.

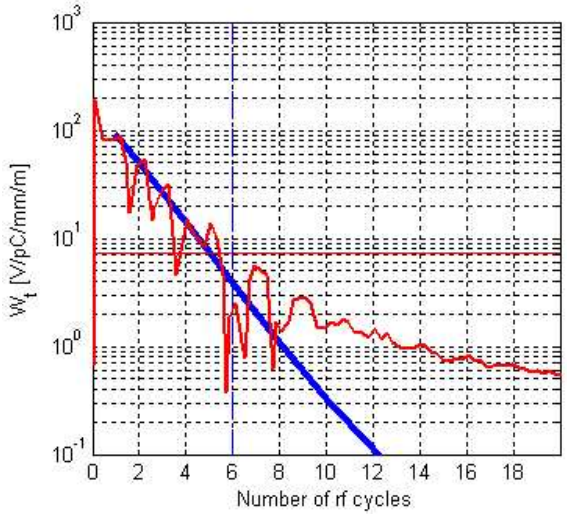

Figure 7: Envelope of the wake of the first (blue) lowest dipole modes, as well as of the total wake (red) in the optimum structure.

4 Injector Complex systems

4.1 Layout of the CLIC injector complex

The design of the injectors for CLIC is based on a central complex housing all the subsystem to prepare the main beams subsequently transported via two long transfer lines to the starting point of each Main linac at the extremities of the collider facility (see Fig. 8). The base line design assumes unpolarized positrons and polarized electrons. The subsystems will be briefly described below, for a more detailed description see [9].

4.2 Polarized Electron Source and Pre-injector

In order to provide a reasonable budget of beam losses in the whole complex, the polarized electron source is designed to deliver $4.4 \cdot 10^9$ electrons with 80% polarization to the entrance of the pre-damping ring (see Table 3). The polarized beam is produced using a high-voltage DC photo injector. A laser which provides already the final time structure of the beam illuminates a strained superlattice GaAs cathode situated in a 120-200 kV high voltage gun. The gun should deliver 312 bunches of 0.9 nC (nominal CLIC bunch charge plus 50% margin) with a bunch repetition frequency of 2 GHz at a repetition rate of 50 Hz.

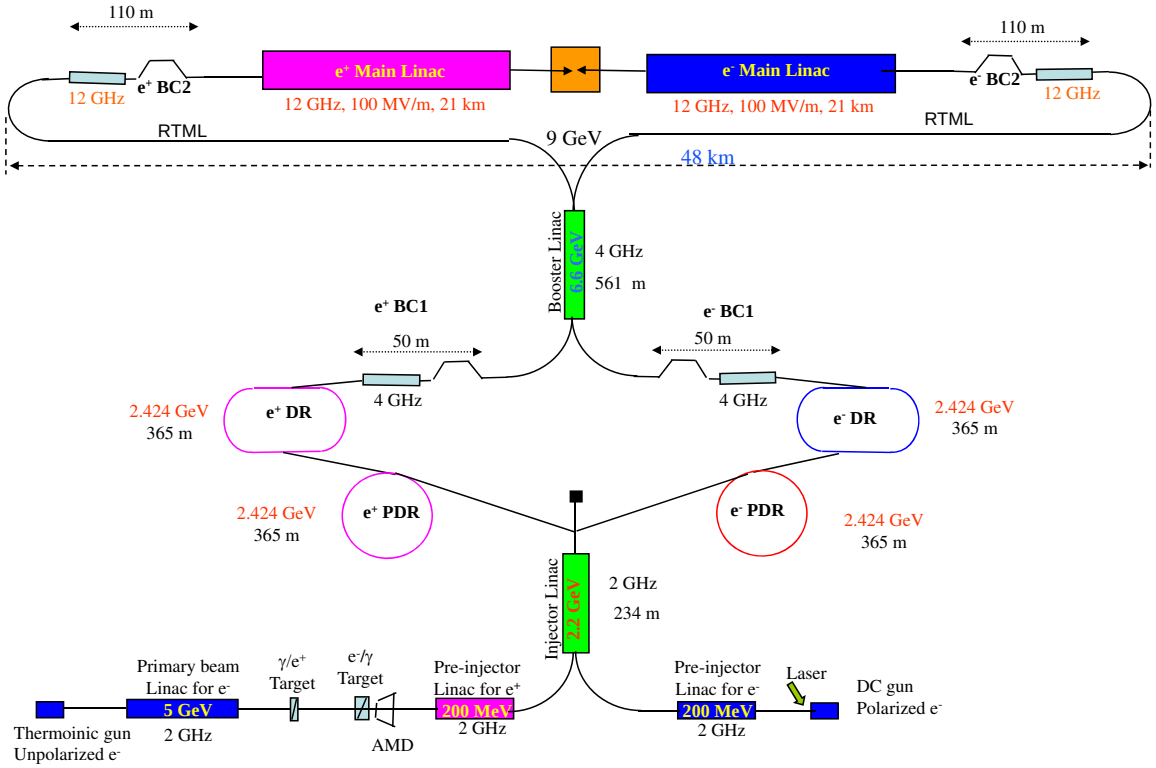

Figure 8: Schematic layout of the CLIC main beam injector complex.

A 2 GHz L-band linac will accelerate subsequently the polarized electrons to 200 MeV followed by a 2.2 GeV linac at the same frequency shared with the positron source. In this Injector Linac [10], the most stringent constraints on the design are set by the positron beam, which has by far the largest transverse emittance. The proposed optics is based on a FODO lattice wrapping the first accelerating structures, followed by a succession of quadrupole triplets and accelerating structures for the rest of the Injector Linac. The linac will operate at a loaded gradient of 15 MV/m and uses standard focusing elements. Beam loading compensation will be done by delayed filling or by direct shaping of the rf pulse in case of an rf pulse compression system. Particle tracking studies suggest that there is practically no emittance growth along the Injector Linac, assuming only short-range wakefields.

The spin has to be vertical at the entrance of the damping rings in order to preserve the polarization therefore the electron injector needs to provide a possibility to adjust the spin.

With the exception of the peak current the key parameters of this source have been achieved in existing or past polarized electron sources [11, 12].

4.3 Positron Source

The baseline positron source is based on a tungsten single crystal target to profit from an enhanced positron yield due to the channeling process. The large number of photons is then converted into e+/e- pairs in the same crystal or in an amorphous target. Such method was successfully tested at CERN [13]. For CLIC, an electron beam of 5 GeV with beam size of 2.5 mm (rms) is sent to a crystal which is 1.4 mm thick oriented along the $<111>$ axis. It produces photons and charged particles (e- and e+). The latter are swept with a dipole magnet downstream the crystal. The photons are sent to an amorphous target situated 2 meters downstream the crystal. Simulations show that a yield of 0.9 e+/e- is achievable with this configuration of targets [14, 15].

An Adiabatic Matching Device (AMD) with a magnetic field tapering from 6 T to 0.5 T over 50 cm is used to match the positron beam to the first accelerating structure. A large acceptance L-band linac with solenoid focusing will accelerate the positron to 200 MeV followed by the 2.2 GeV linac which is also used for electrons [10].

Taking into account the acceptance of the Pre-Damping ring (70% injection efficiency only due to the larger energy spread for the e+), one needs $6.4 \cdot 10^9$ e+/bunch at the entrance of the Pre-Damping ring (see Table 3). Considering the positron losses in the injector linacs and the positron production yield $7.5 \cdot 10^9$ e-/bunch are needed on the positron target at 5 GeV. These electrons are provided by a classical thermionic gun and a 2 GHz accelerator.

An alternative scheme using a conventional positron production target at 2 GeV is as well feasible but would require three parallel target stations due to the energy density limitation of these targets.

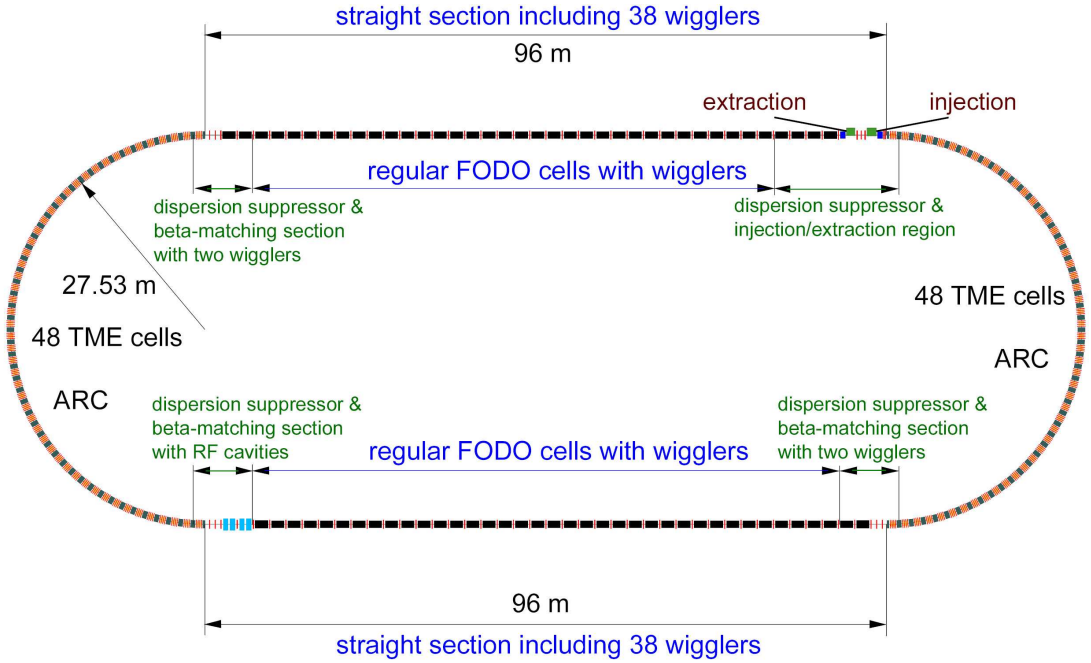

Figure 9: Schematic layout of the CLIC damping rings [16].

4.4 Pre-damping rings and Damping rings

Since the 2005 note documenting the CLIC parameters, the design and layout of the CLIC damping rings (DR) have not substantially changed (see Fig. 9). On the other hand, the performance of the DR was further optimized to achieve the target normalized emittances at their output. These studies were principally documented in the PhD thesis of M. Korostelev [16] and describe the baseline of the damping rings' design as of this date. At a later stage, and in view of the change in the main CLIC structures, the impact of the imposed new parameters in the DR output emittances was studied but without a further optimization of the DR performance. The old and actual DR parameters are displayed in Table 2.

The electron and positron bunches with energy of 2.424 GeV are injected into the two DR whose layout is of racetrack form. The two arcs are filled with 1.8m long theoretical minimum emittance (TME) cells and the straight sections contain FODO cells with damping wigglers. A zone for injection and extraction is also included after the dispersion suppressor of one of the arcs. The total length of the ring was slightly increased to 365.2m by raising the total number of TME cells to 100 and reducing some space in the dispersion suppressors. The phase advance per TME cell was kept to 210° in the horizontal and 90° in the vertical plane, providing a detuning factor of 1.8 with respect to the minimum emittance of the corresponding TME cell. The chromaticity is controlled by a pair of sextupole families.

A further reduction of the emittance is achieved with the inclusion of 76 damping wigglers. With the previous set of parameters, the target transverse emittance was not achieved due to the strong effect of IBS which increases the horizontal output emittance by almost a factor of 5 with respect to the equilibrium emittance. It was thus necessary to choose higher wiggler fields, above the saturation level of iron dominated magnets, and shorter wiggler wavelengths. The impact of these two parameters in the emittance is shown in the contour plot of Fig. 10 where the curves inscribing the same colors correspond to the same emittance ranges after including the effect of intra-beam scattering (IBS). In the present design, the wiggler field is of 2.5 T which necessitates super-conducting materials for achieving it, with a period of 5 cm [17]. In this respect, the achieved normalized horizontal emittance at the damping rings output dropped below 400 nm.

Apart from the impact in the beam sizes at the output of the DR, the change in the wigglers' parameters triggered the increase of the energy loss per turn and the decrease of the damping times in all 3 dimensions. In this respect, the RF voltage had to increase in order to provide enough energy recovery while keeping the longitudinal emittance below 5000 eVm. Furthermore, the vertical tune of the DR had to be reduced by a unit to accommodate the wigglers' field change.

The previous parameter set included the influence of misalignments on the vertical emittance which was considered to be dominated by coupling with a coupling coefficient of 0.6, fixed by the target emittance at the DR output. A further detailed study of alignment tolerances and their influence on the vertical emittance was undertaken [16].

Parameter [unit]	symbol	old value (2005)	new value (2007)
beam energy [GeV]	E_b	2.424	2.424
circumference [m]	C	360	365.2
bunch population [10^9]	N	2.56	3.72 $\times$1.1
bunch spacing [ns]	$T_{\rm sep}$	0.533	0.5
bunches per train	$N_{\rm b}$	110	312
number of trains	$N_{\rm train}$	4	1
store time / train [ms]	$t_{\rm store}$	13.3	20
rms bunch length [mm]	σ_z	1.547	1.53
rms momentum spread [%]	σ_δ	0.126	0.143
final hor. emittance [nm]	$\gamma\epsilon_x$	550	381
hor. emittance w/o IBS [nm]	$\gamma\epsilon_{x0}$	134	84
final vert. emittance [nm]	$\gamma\epsilon_y$	3.3	4.1
coupling [%]	κ	0.6	0.13
vertical dispersion invariant	$\mathcal{H}_y$	0	0.248
no. of arc bends	$n_{\rm bend}$	96	100
arc-dipole field [T]	$B_{\rm bend}$	0.932	0.932
length of arc dipole [m]	$l_{\rm bend}$	0.545	0.545
beam pipe radius in arc [cm]	$b_{\rm arc}$	2	2
number of wigglers	$n_{\rm wiggler}$	76	76
wiggler field [T]	$B_{\rm wiggler}$	1.7	2.5
length of wiggler [m]	$l_{\rm wiggler}$	2.0	2.0
wiggler period [cm]	λ_w	10	5
vertical wiggler half gap [cm]	b_w	0.6	0.5
momentum compaction	α_c	0.796×10^{-4}	0.804×10^{-4}
synchrotron tune	Q_s	0.005	0.004
horizontal betatron tune	Q_x	69.82	69.84
vertical betatron tune	Q_y	34.86	33.80
RF frequency [GHz]	$f_{\rm RF}$	1.875	2
energy loss / turn [MeV]	U_0	2.074	3.857
RF voltage [MV]	$V_{\rm RF}$	2.39	4.115
hor., ver., long. damping time [ms]	τ_x, τ_y, τ_s	2.8, 2.8, 1.4	1.5, 1.5, 0.76
revolution time [μs]	$T_{\rm rev}$	1.2	1.2
repetition rate [Hz]	$f_{\rm rep}$	150	50

Table 2: CLIC damping rings parameters as registered in the 2005 note and new parameters after the main RF structure redesign.

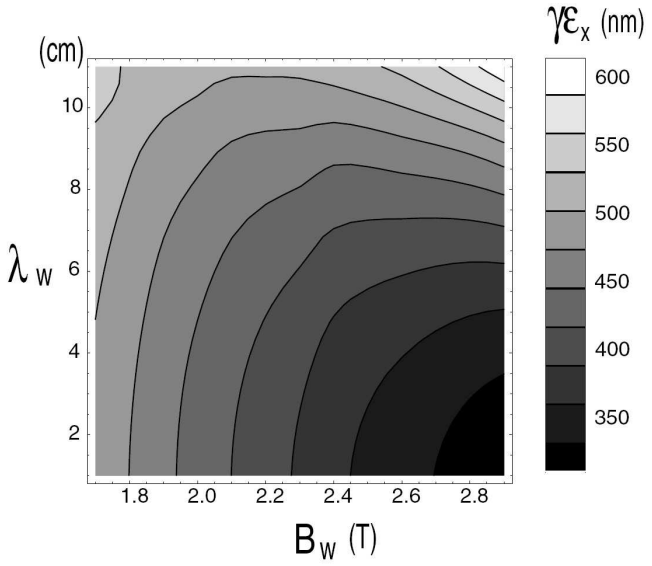

Figure 10: Contour plot displaying the dependence of DR horizontal emittances with respect to the period $\lambda_{\rm W}$ and field $B_{\rm W}$ of the damping wigglers [16]. The effect of IBS in the emittance blow-up is included.

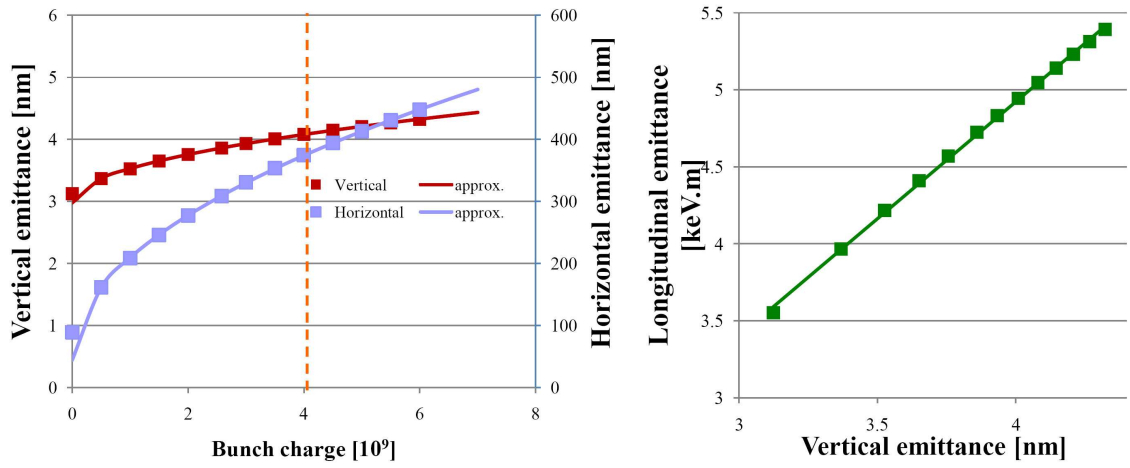

Figure 11: Horizontal and vertical emittance dependence on bunch charge (left) and dependence of the vertical emittance with the longitudinal one (right).

This study showed that the vertical emittance growth is dominated by vertical dispersion and less by coupling. The vertical emittance values quoted in the latest parameter set are taking into account this effect by including a non-vanishing dispersion invariant for the vertical plane as well, and integrating the complete set of coupled differential equations for evaluating the effect of IBS.

The change of the CLIC RF structure design parameters, had a major impact on the bunch charge which increased by a factor of 1.6 taking into a account a 10% margin for losses in the downstream injector systems. Figure 11 presents the dependence of the DR transverse emittances with respect to the bunch charge and the relation of the vertical emittance with the longitudinal one [18]. The horizontal emittance scales linearly with the square root of the bunch charge (for high charges) and inversely with the square root of the longitudinal emittance. The vertical emittance has a much weaker dependence on the bunch charge and scales linearly with the longitudinal one. So the impact of the higher charge on the horizontal emittance was small and it could be kept well within the target values. The same was true for the vertical emittance, which was also kept within the budget.

The previous injection and extraction procedure was based on an interleaved bunch train scheme where two pairs of two bunch trains were injected and extracted simultaneously and than recombined with the help of a delay loop and RF deflectors. This scheme had the interesting feature of doubling the bunch spacing in the DR, thus reducing the effect of electron cloud and fast ion instabilities. This solution was abandoned due to its complexity. Furthermore, the change of the parameters in the main CLIC cavities increased the bunch spacing to almost the same level as in the case of the interleaved bunch scheme. The number of bunches with the above mentioned bunch spacing fill 13% of the rings. The reduction of the repetition rate to 50Hz provides a long time of 20 ms for the transverse emittances to reach their equilibrium. Note finally the increase of the RF frequency to 2GHz and the total RF voltage to 4MV.

Although a detailed study of collective effects has still to be undertaken, a first estimate of the effect of the new parameters on the electron cloud was performed [19], and showed that ante-chambers are essential in both wigglers and dipoles to absorb 99.9% of the photon flux. The secondary electron emission yield has to be less than 1.3 in order for the beam to remain stable and a major program of material tests and surface treatments will be followed in order to find an adequate vacuum chamber design.

4.5 Booster Linac, Bunch Compressors and Beam Transport to the Main Linac

The requirements of the beam transport from the damping rings to the main linacs are to compress bunches to their final bunch length, to accelerate the beam to 9 GeV and to preserve the excellent beam quality obtained in the damping rings.

The design of the bunch compression is being studied in the framework of EUROTeV [20]. The bunch compression is done in two stages, in front of the Booster linac to provide an appropriate bunch length for acceleration and finally at the entrance to the Main linac. Each chicane consists of four magnets and compresses bunches first by a factor nine and finally by a factor four [21]. They have been designed taking into account the effect of coherent synchrotron radiation. The first stage uses 4 GHz rf structures to introduce the energy chirp while the second stage uses a 12 GHz system. The 270 degree turn-around loop at the beginning of each linac was designed carefully to preserve the emittance taking into account CSR and ISR effects.

For the 6.6 GeV Booster linac a succession of triplets and accelerating structures is proposed. There is the choice

Parameter	Unit	PDR e+	PDR e-	Main linacs
Energy	GeV	2.424	2.424	9
No/bunch	10^9	6.4	4.4	3.72- 4
Bunch length (rms)	mm	5	1	0.044
ΔE/E (rms)	%	3.5	0.1	1.3
$\gamma\epsilon_x$	nm.rad	$9.3 \cdot 10^6$	10^5	600
$\gamma\epsilon_y$	nm.rad	$9.3 \cdot 10^6$	10^5	10

Table 3: Beam parameters at the entrance of the Pre-Damping rings and Main Linacs

between a 2 GHz and a 4 GHz linac (it has to be a multiple of the 2 GHz bunch repetition rate). The 4 GHz option could benefit from a higher gradient ($G_{\rm loaded}$ = 30 MV/m) and would be therefore a factor two shorter than the L-band version. However detailed simulations have to confirm if the wakefields of such a linac would be acceptable. The two 24 km long transfer lines towards the turn-arounds require a vacuum in the order of 10^{-10} mbar to avoid the fast ion-beam instability.

Table 3 summarizes the beam parameters required at different key locations within the injector complex.

5 Main Linacs

Due to the high RF frequency the longitudinal and transverse wakefields in the CLIC main linac are quite strong. The main linac lattice has therefore to be designed with special attention to the minimisation of the effects caused by these wakes. The lattice for the previous parameter set has been derived in a careful optimisation of the focusing strength along the linac, see reference [22].

All main linac components are mounted on girders with a length of 2.01 m. Five different girder types exist. The first type supports eight accelerating structures (each 23 cm long). In the other types the first two, four, six or all eight structures are removed and replaced with a quadrupole of similar length. The lattice consists of twelve sectors of FODO cells, with a constant quadrupole spacing and phase advance per cell. The cell length in each sector is chosen to be proportional to $\sqrt{E}$. This choice balances dispersive and wakefield effects that are both harmful to the beam emittance. It also keeps the fill factor roughly constant along the main linac. The matching between sectors is achieved by adjusting the strength of seven quadrupoles.

In the linac, the beam is accelerated off the crest of the RF wave. This is necessary since the single bunch longitudinal wakefields introduce an energy spread in the beam. The fields induced by the beam head is decelerating the beam tail. If the beam arrives slightly before the crest of the accelerating RF, the tail will be accelerated more than the head. This can be used to counterbalance the wakefield induced effect. For the old parameters it was required that the beam has an energy spread of less than 1% full width at the end of the linac and that the beam is accelerated by not more than 15° off-crest. These constraints have been used to determine for each structure the minimum bunch length as a function of the bunch charge. For the new parameters exactly the same procedure was used.

The transverse wakefields of the structure have been the main source of emittance growth for the old parameter set. This growth depends on the lattice design. Since the old design had been optimised thoroughly to minimise the wakefield effects, it was assumed that no better solution can be found for the new lattice, if one does not want to decrease the fill factor. Consequently the constraint was set that the new beam should see the same transverse wakefield effects as the old one. As a simple measure for this, the amplitude of the wake kick over a bunch length was used. It was required that $N \cdot w(2\sigma_z)$ be the same for the old and new parameters.

The linac components are pre-aligned by the survey system and then finally aligned using beam-based alignment methods. The following procedure is envisaged:

- All beam line elements are pre-aligned by the survey system with a very high accuracy of the order of $10\ \mu$m.
- Simple one-to-one steering is used to centre the beam in all BPMs and to make it pass the linac with essentially no losses.
- Beam-based alignment is used to align beam-position monitors and quadrupoles. Different methods can be chosen, the default is to use dispersion free steering. In this procedure beams with different energies are used to determine and remove the dispersion in the lattice.
- The accelerating structures are aligned to the beam. Each of them is equipped with a wakefield monitor that can determine the beam offset in the structure. The end-points of the girders can be moved in order to minimise the mean offset of the structures to the beam.
- If necessary, emittance tuning knobs can be used to further improve the emittance. In this method the final emittance is measured and sets of structures are moved transversely with the goal to minimise the monitored emittance.

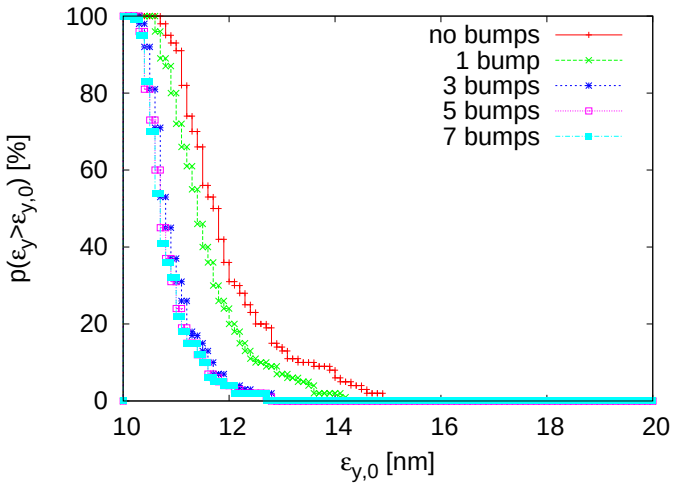

Figure 12: The probability distribution for the emittance growth $\Delta\varepsilon$ after beam-based alignment. The cases where emittance tuning bumps are used in addition are also shown.

For the new parameters the wakefield induced emittance growth has been reduced. This is mainly due to the tighter requirement for the accuracy of the wakefield monitor in the accelerating structures. Previously, an accuracy had been assumed of $10\,\mu$m for 50 cm long structures, while for the new parameters $5\,\mu$m for 23 cm long structures is targeted. This leads to a reduction of the wakefield induced emittance growth of a factor eight. Further reductions were achieved by reducing the target for the wakefield kick over the bunch. In addition the emittance growth budget in the main linac has been increased. For the previous parameter set the use of beam-based alignment had not been sufficient to achieve the required performance, the use of emittance tuning knobs had been mandatory. For the new parameters this is no longer the case. Beam-based alignment alone yields the required performance with a probability of more than 90%. Tuning knobs can be now considered a reserve measure. Figure 12 shows the probability of achieving the emittance goal for beam-based alignment alone and for the subsequent application of emittance tuning knobs [23].

In addition to the single bunch wakefields, another concern are the multi-bunch transverse wakefields, which can lead to multi-bunch beam break-up. Simulations have shown that the additional effects from the multi-bunch wakefields can be neglected in comparison to the single bunch effects for a transverse wakefield amplitude of $20\,\mathrm{kV/pCm^2}$ and a bunch charge of 4×10^9. For a given structure design, the multi-bunch wakefields can be reduced by spacing the bunches further apart. In the optimisation (see section 3), a constraint $w(N_s\lambda_{RF}) \cdot N/\,4 \times 10^9 \cdot 150\,MV/G \leq 10\,\mathrm{kV/pCm^2}$ (see Eq. 1) has been respected. The multi-bunch effects should therefore be acceptable as a first simulation of the multi-bunch beam break-up indicates.

6 Beam Delivery, Collimation and Backgrounds

Since 2005 the CLIC Beam Delivery System (BDS) has experienced various modifications. A new diagnostics section has been introduced prior to the energy collimation. The Final Focus System (FFS) has undergone modifications in the beam line optics to achieve a minimum beam size at the IP. A reduction of the FFS length has also been explored with two goals: finding the optimum performance and shortening the tunnel. In the following we describe the different subsystems of the BDS, a detailed description can be found in [24]. All the lattices on this paper and, in general, all CLIC lattices can be found at the web repository [25].

6.1 The new diagnostics section

The goals of the diagnostics section are:

1. Compensation of transverse coupling errors
2. Emittance measurement
3. Energy measurement
4. Polarization measurement

To address the first two points the beam line shown in Fig 13 has been appended to the beginning of the BDS. Four skew quadrupoles are located at the peaks of the β_y in the first 100 m and four beam size monitors are located at the rest of the β_y peaks. These β_y have been chosen so that the vertical beam size is 1 μm for $\epsilon_y = 20$ nm. Present laser wire technology can measure this beam size with a 10% resolution. Preliminary simulations [26] have shown that the resolution on the final emittance measurement is below the 5% level [27].

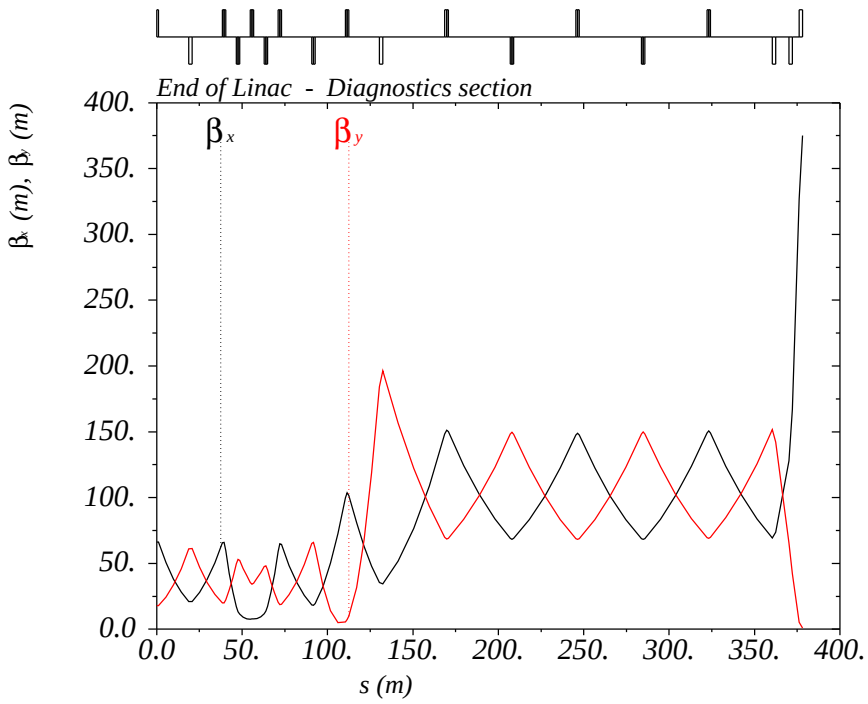

Figure 13: Layout and optics of the diagnostics CLIC section. The peaks of the vertical beta function correspond to 1 μm beam size for $\epsilon_y = 20$ nm.

The energy measurement has been conceived such that no extra space will be required. The first dipole of the collimation section is used as spectrometer in conjunction with BPM pairs at both sides of the dipole. Assuming the relative calibration error of the dipole being 10^{-4} and the BPM resolution being 100 nm, the relative error on the energy measurement is about 4×10^{-4}. This performance should be enough for machine operation however there is no specification from the detector side.

The polarization measurement has not been addressed yet but it is a fundamental measurement for the CLIC physics. This is typically achieved by colliding the beam with a laser and detecting the backscattered electrons. To separate these electrons from the beam a bending dipole is required after the laser. It should be considered if this laser could be placed before the spectrometer dipole used for the energy measurement.

This new diagnostics section has increased the total length of the BDS by 370 m. Fig. 14 shows the BDS layout and optics having a total length of 2.75 km. For this illustration a new FFS has been used which is about 100 m shorter than in the previous study (see section 6.3). If the length of the system becomes a critical parameter it could be possible to fill the empty spaces in the first 100 m of the diagnostics section with cavities, thus shortening the linac by the same amount.

6.2 The collimation section

No changes have been done to the collimation section. However the new beam parameters lay on the edge of the collimation survival estimates after the collision of a full train. This has been inferred from [28], where Be collimators survive the impact of a train with half the charge of the present beam. Therefore, studies have to be pursued to devise a robust collimation system.

6.3 The Final Focus System

The CLIC FFS has recently undergone numerous optimizations, detailed descriptions can be found at [29, 24]. The first optimization was based in the minimization of the IP spot sizes by small modifications of the optics, like adding non-linear elements, reducing dispersion along the FFS, etc. The second optimization targeted the length of the system. Scaling down the FFS length with constant IP beta functions comes with a reduction of chromatic aberrations. This also has the advantage of shortening the tunnel. These two sets of optimizations led to two different FFS with different lengths and L* (free distance to the IP). The two lattices perform very similarly in terms of peak luminosity. This is in accordance with the observation that for the new beam parameters (σ_z=44 μm and $\epsilon_y = 20$ nm) the luminosity in the energy peak is saturated, i.e., further reductions of the horizontal spot size do

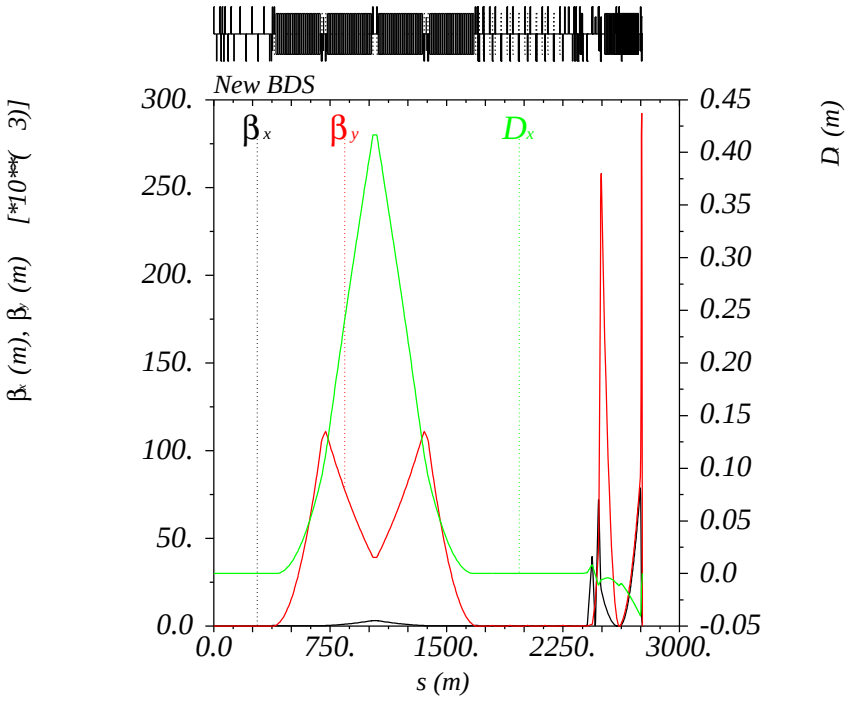

Figure 14: Layout and optics of the full CLIC BDS.

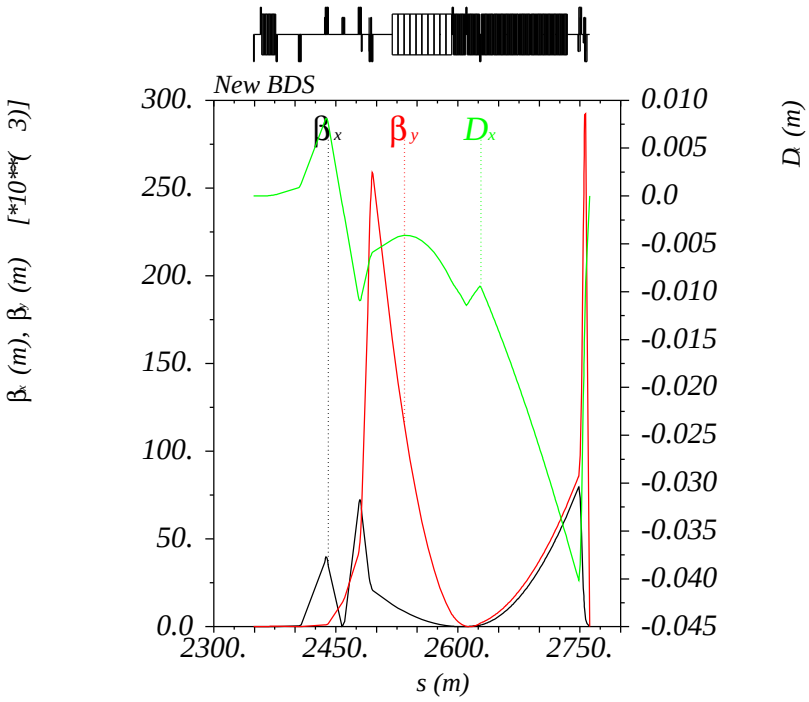

Figure 15: Layout and optics of the CLIC FFS.

not increase the peak luminosity due to the enhanced beamstrahlung. The shorter FFS is shown in Fig. 15. All the BDS parameters for these two lattices are listed in Table 4 together with the old CLIC parameters for comparison. The future work on the FFS will be oriented towards the optimization of the lower energy options, mainly 500 GeV.

parameter	Symbol	old value	new value 1	new value 2	unit
IP free length	L^*	4.3	4.3	3.5	m
FFS length		550	550	460	m
CS length		2.0	1.92	1.92	km
DS length		0	370	370	m
BDS length		2.5	2.84	2.75	km
bunch population	N	2.56	4	4	10^9
number of bunches / train	N_b	220	312	312	
horizontal emittance	$\gamma\epsilon_x$	0.68	0.68	0.68	μm
vertical emittance	$\gamma\epsilon_y$	0.01	0.02	0.02	μm
horizontal IP beta function	β_x^*	7	5.6	6.9	mm
vertical IP beta function	β_y^*	90	81	68	μm
horizontal IP core spot size	σ_x^*	60	44	45	nm
vertical IP core spot size	σ_y^*	0.70	0.92	0.90	nm
ideal horizontal IP spot size	σ_{x0}^*	37	38	40	nm
ideal vertical IP spot size	σ_{y0}^*	0.50	0.73	0.67	nm
bunch length	σ_z	30.8	35	44	μm
crossing angle	θ_c	20	20	20	mrad
repetition rate	$f_{\rm rep}$	150	50	50	Hz
Total luminosity	L_t	3.6	6	6	10^{34} cm^{-2}s^{-1}
Peak luminosity (in 1% of E)	$L_{1\%}$	-	2	2	10^{34} cm^{-2}s^{-1}

Table 4: Beam-Delivery System Parameters

6.4 Luminosity and Beam-Beam Effects

The charge density in the bunches at the interaction point is so high that the colliding beams focus each other strongly. The transverse beam size is even significantly decreasing during the collision. This process increases the luminosity but it also leads to the emission of beamstrahlung due to the bending of the particle trajectories. The average energy of the emitted photons is very high – of the order of 10% of the particle energy – and also the probability of emission is high – of the order of one photon per beam particle. The fact that particles collide after emission of beamstrahlung leads to the development of a luminosity spectrum. For the physics mainly the part of the luminosity close to the nominal centre-of-mass energy is relevant. Hence some part of the luminosity will not be useful any more. For otherwise fixed beam parameters the luminosity is proportional to $1/(\sigma_x\sigma_y)$ while the beamstrahlung increases as $1/(\sigma_x+\sigma_y)$. In all linear colliders one therefore uses flat beams with $\sigma_x \ll \sigma_y$, which minimises the product but maximises the sum of the two beam dimensions. One therefore aims to minimise σ_y which will lead to more luminosity in all cases. The choice of σ_x however is a trade-off between more luminosity (smaller σ_x) and a better luminosity spectrum (larger σ_x).

The luminosity is determined by integrated simulation including the beam delivery system and the beam-beam effects. First, a beam is generated that has the transverse emittances that correspond to the target values at the end of the main linac, namely $\epsilon_x = 660\,\mathrm{nm}$ and $\epsilon_y = 20\,\mathrm{nm}$. The energy spread of the beam is included in full detail and including correlations introduced by the main linac. The beam is then tracked through the beam delivery system with no imperfections. In order to account for such imperfections, the vertical beam size is then increased by 20%. Finally, the beam-beam interaction is simulated. With this procedure, one finds the luminosity to be about $6\times10^{34}\mathrm{cm}^{-2}\mathrm{s}^{-1}$ and the luminosity above 99% of the nominal centre-of-mass energy to be about $2\times10^{34}\mathrm{cm}^{-2}\mathrm{s}^{-1}$.

6.5 Background

An introduction to the different types of background can be found in [2]; the values listed in the reference are for an older parameter set. The background level at the IP for the present parameters is given in Table 15.

6.6 Post-collision line

In addition to the large energy spread of the beam particles after collision, the previously mentioned beamstrahlung photons emitted in the strong fields during collision can turn into e^+e^- coherent pairs. A careful design of the post-collision line must therefore be performed to transport all outgoing beams from the interaction point to the dump, with as small losses as possible. A schematic layout of this beam line is shown in Figure 16 [30].

In a first step, 20 m downstream of the interaction point, the CLIC post-collision line separates the various components of the outgoing beam in four vertical extraction magnets, which provide a total bending angle of 3.2 mrad at

1.5 TeV. One way to keep simultaneously the beam losses and the transverse dimensions of the extraction magnets at a reasonable level is to install 90 cm long collimators between them. Their purpose is to absorb some of the particles found in the low-energy tails, which are far away from the reference beam trajectory. The left-hand side of Figure 17 shows the transverse beam profiles, as obtained in the separation region, 49 m downstream of the interaction point.

Following their physical separation from the other beam components, the particles of the coherent pairs with the wrong-sign charge are immediately brought to their dump. The energy spectrum of the coherent pairs can be derived from the vertical distribution of this wrong-sign charged beam. As for the disrupted beam and the beamstrahlung photons, they are transported in the same vacuum pipe to a common dump. The bend provided by the four extraction magnets is followed by a bend in the opposite direction, which is provided by four C-type magnets, in order to eventually have $D'_y = 0$. All beamstrahlung photons and charged particles with more than 16% of the nominal beam energy pass through the vertical chicane and reach the end of the post-collision line, 75 m downstream. The other particles are absorbed in the lower part of the instrumented dump of the coherent pairs, which is placed in front of the C-type magnets. The right-hand side of Figure 17 shows the vertical beam profiles, as obtained at the end of the post-collision line, 150 m downstream of the interaction point.

An accurate analysis of the final transverse beam profiles, the flux of beamstrahlung photons and coherent pair allows to derive some relevant information on the e^+e^- collisions. In particular, small vertical offsets in position and/or angle between the incoming beams may affect the disruption process and can then be identified by measuring the displacement and/or the distortion of the outgoing beams. Note that these offsets may lead to some additional losses along the post-collision line, however these only occur in the collimators and in the intermediate dump. Four post-collision diagnostics tools aimed at monitoring the disruption process are proposed [31]: tail

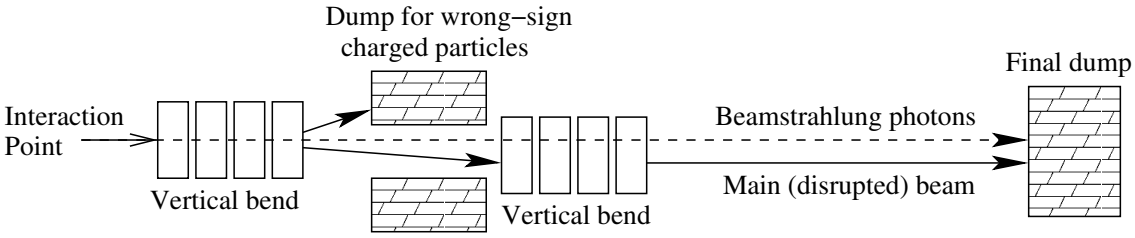

Figure 16: Schematic layout of the CLIC post-collision extraction line, where the arrows show the path of the beamstrahlung photons and of the charged particles (disrupted beam and e^+e^- coherent pairs).

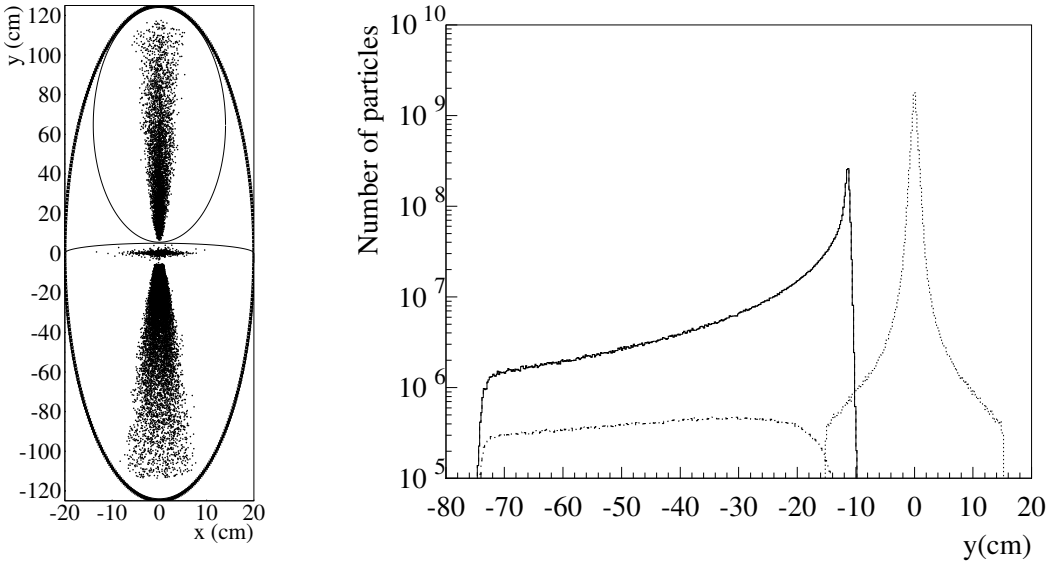

Figure 17: Transverse beam profiles obtained in the separation region, 49 m downstream of the interaction point (left). Vertical profiles for the charged beam (full line), including the particles of the coherent pairs with the right-sign charge (dashed line), and for the beamstrahlung photons (dotted line), as obtained at the end of the post-collision line, 150 m downstream of the interaction point (right).

monitors that are embedded in the collimators, measurement of the flux and vertical profile of the wrong-sign charged particles of the coherent pairs at the intermediate dump, beamstrahlung monitor based on the detection of the Cerenkov light emitted by muons behind the main dump, and an interferometric set-up to monitor water temperature profiles in the dump.

Analytical calculations and numerical simulations of the energy deposition, the temperature increase due to the beam impact and the stresses in the window between the accelerator vacuum and the beam dump at the end of the CLIC post-collision line were performed [32]. Similarly to the design considered for the LHC dump window, we propose a thick (1.5 cm) layer of carbon-carbon composite (SIGRABOND 1501G) and a thin (0.2 mm) leak-tight foil made of Aluminum. This material both yields a small thermal stress and allows to quickly transport away the heat resulting from the beam impact. In our design, the thickness of the window remains significantly smaller than one radiation length (which ensures that only ionization losses occur during the beam passage), but still large enough to withstand the pressure difference. The window has a race-track shape with a straight line length of 54 cm and two half-circles with a radius of 20 cm. In the worst case scenario (with a failure of all magnetic elements along the post-collision line), the undisrupted beam covers an area of 2.5 mm^2 and hits the window 4 cm above the centre of the upper circle. The thermal and mechanical constraints induced are more relaxed than for the LHC dump window.

7 Linac Module Layout and PETS (Power Extraction Transfer Structure)

7.1 Module Layout

The CLIC two-beam configuration along most of the length of the main and drive linacs (excluding special diagnostic sections for example) consists of repeated 'modules' [33]. Each module contains four power extraction structures (PETS, see section 7.2), feeding two accelerating structures each, and two drive-beam quadrupoles, as a very dense lattice is required for the low-energy drive beam. The module is mounted on each alignment girder, and a schematic view of this layout is shown in Fig. 18. Space for quadrupoles in the main linac is made by leaving out two, four six or eight accelerating structures and suppressing the corresponding PETS (see Fig. 19).

The stagger between the two linacs is made to give the correct relative RF to beam timing. The module length (2010 mm) is determined mainly by the length of accelerating structures (230 mm) and the fact that a PETS feeds two structures (a number which depends on the high-power capability of the PETS which will be determined in the CTF3 12 GHz experimental program). Drive linac beam dynamics simulations show that the drive beam quadrupole spacing must be about 1 m with a quadrupole length of about 270 mm for sufficient strength. The remaining space is then available for two PETS and the BPM which is just sufficient. A 30 mm length has been reserved for inter-girder connections, currently under study. For the module integration (see Fig. 20), the main requirements for the different sub-systems (alignment, supporting, stabilization, cooling and vacuum) have to be taken into account. For example the required stable thermal behavior and the tight tolerances of accelerating structures (the requirements for the accelerating structure pre-alignment is 0.014 mm at 1σ) in the CLIC linac directly affect the sizing and integration of the cooling system.

A few modules with main beam and drive beam quadrupoles only are required in the regions (about 10 m) where each drive beam is fed into and out of a drive beam linac sector.

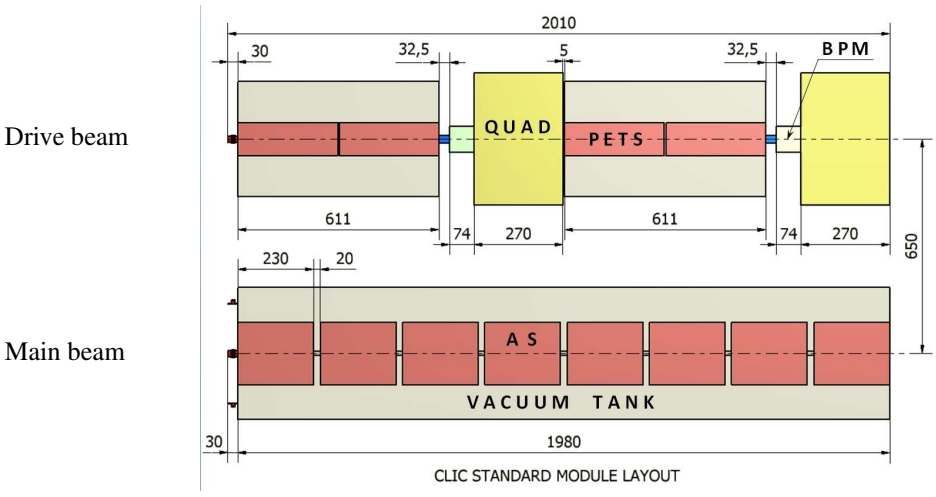

Figure 18: Schematic view of the standard module layout with the drive beam shown on top and the main beam on the bottom.

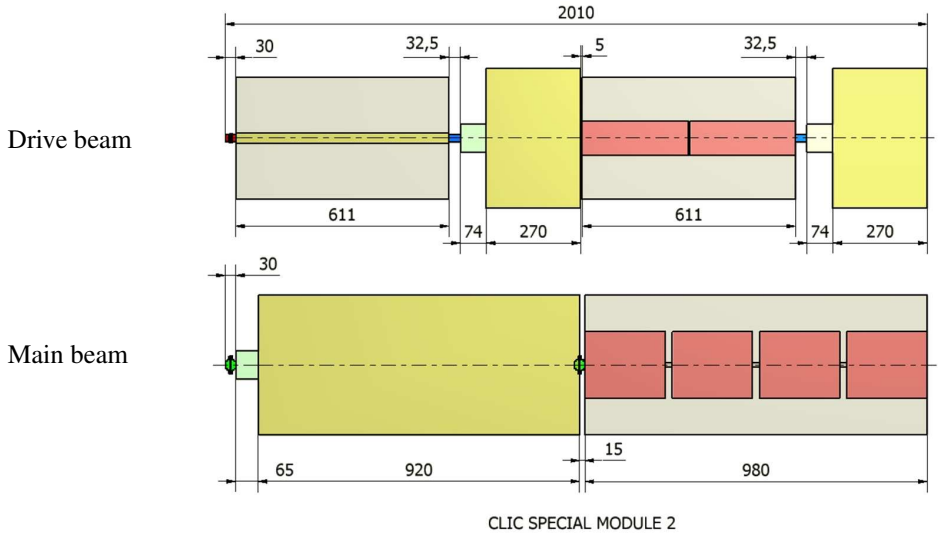

Figure 19: Schematic view of a typical quadrupole module layout (quadrupoles shown in yellow).

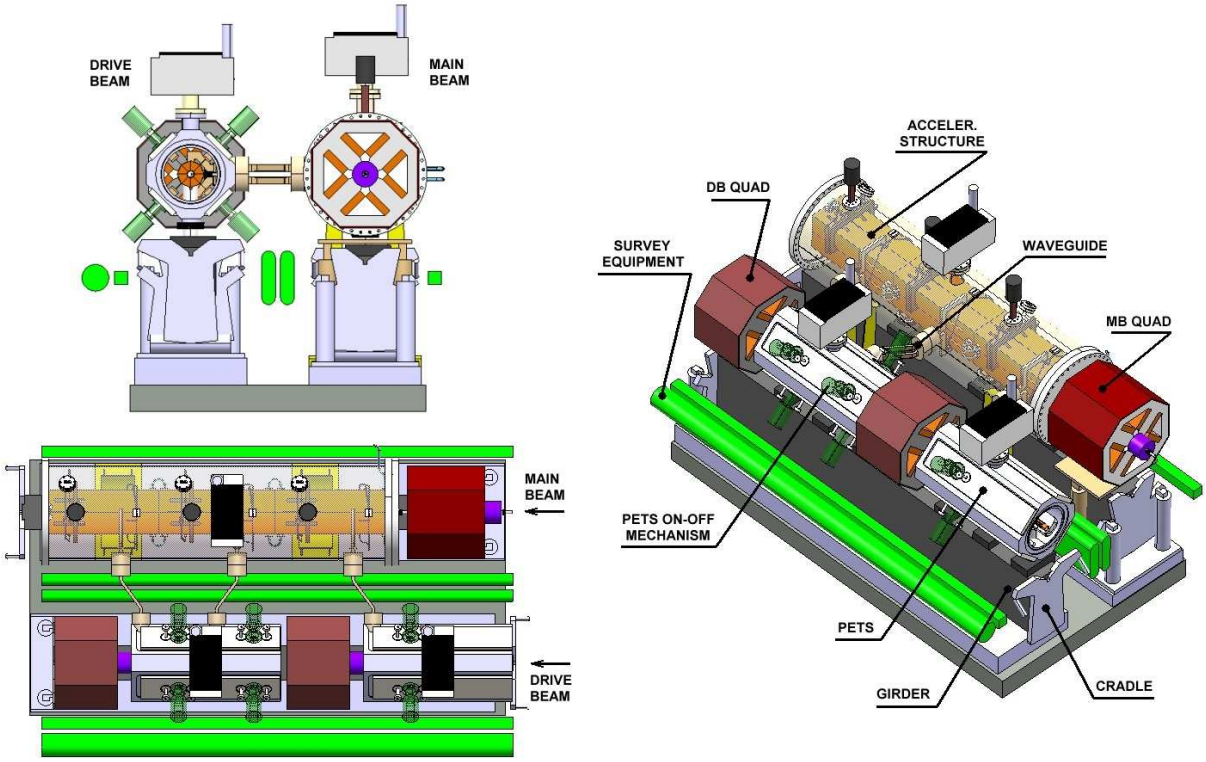

Figure 20: Schematic view of the standard module.

Aperture, mm	23
Phase advance/cell, degrees	90
R/Q, Ohm/m	2295
$\beta = V_g/c$	0.453
Q-factor	7200
Active length, m	0.213 (34 cells)
Drive beam current, A	101
RF power, MW	136

Table 5: The X-band CLIC PETS parameters.

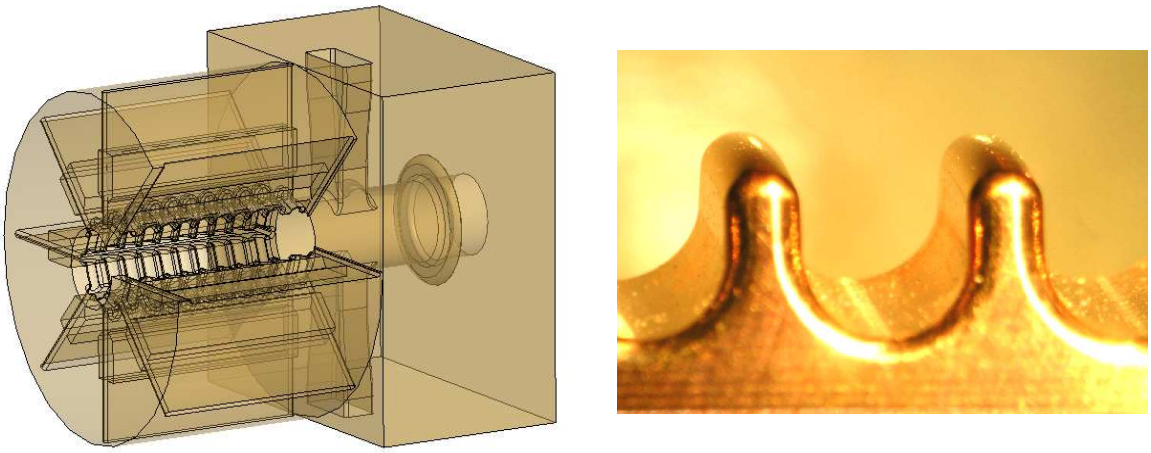

Figure 21: The CLIC PETS general view (left). The view of the PETS single bar period (right).

7.2 CLIC Power Extraction and Transfer Structure (PETS)

The CLIC Power Extraction and Transfer Structure (PETS) is a passive microwave device in which bunches of the drive beam interact with the impedance of the periodically loaded waveguide and excite preferentially the synchronous mode. The RF power produced is collected at the downstream end of the structure by means of the Power Extractor and delivered to the main linac structure.

The layout of the CLIC module is shown in Fig. 20. In this layout, the single PETS should produce RF power for two accelerating structures. The RF power generated by the bunched beam in a constant impedance periodic structure in general can be expressed as:

$$P = I^2 L^2 F_b^2 \omega_0 \frac{R/Q}{4\, V_g} \tag{2}$$

where I is the beam current, L – the active length of the structure, F_b – the single bunch form factor, ω_0 – the bunch frequency, *R/Q* – the impedance per meter length, Q - the quality factor and V_g – the group velocity. At a given frequency and with fixed RF power and beam current, the only free parameters are the structure length and structure aperture. In our case, the PETS active length is limited by the module layout and thus the structure aperture absolute upper limit is well defined (impedance $\propto 1/a^2$). The lower limit for the structure aperture is governed by the RF constraints [34]. In a simple way it can be written as: $a_{PETS} \geq a_{as} \times n_{as}$, where a_{as} is the input aperture of the accelerating structure and n_s is the number of accelerating structures fed by the single PETS. In addition, the choice of the aperture defines the power extraction strategy, which in turn, can influence the active length. As a result of multiple compromises the PETS aperture with a/λ=0.46 was chosen, see Table 5.

In its final configuration, PETS comprises eight octants separated by the damping slots. Each of the slots is equipped with HOM damping loads. This arrangement follows the need to provide strong damping of the transverse modes. In periodic structures with high group velocities, the frequency of a dangerous transverse mode is rather close to the operating one. The only way to damp it is to use its symmetry properties. To do this, only longitudinal slots can be used. These slots also naturally provide high vacuum conductivity for the structure pumping. The upstream end of the PETS is equipped with a special matching cell and the output coupler [35], see Fig. 21. The simulated efficiency of the power extraction from PETS is above 99%, see S-parameters simulated with HFSS [36] in Fig. 22.

Throughout the PETS design, special care was taken to reduce the surface field concentration in the presence of

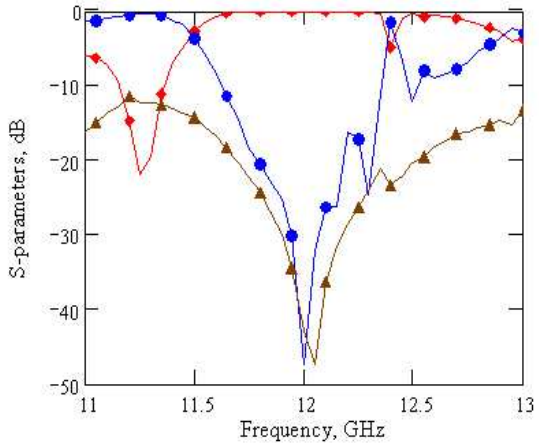

Figure 22: The PETS S-parameters, diamonds -transmission, circles - reflection and triangles - isolation.

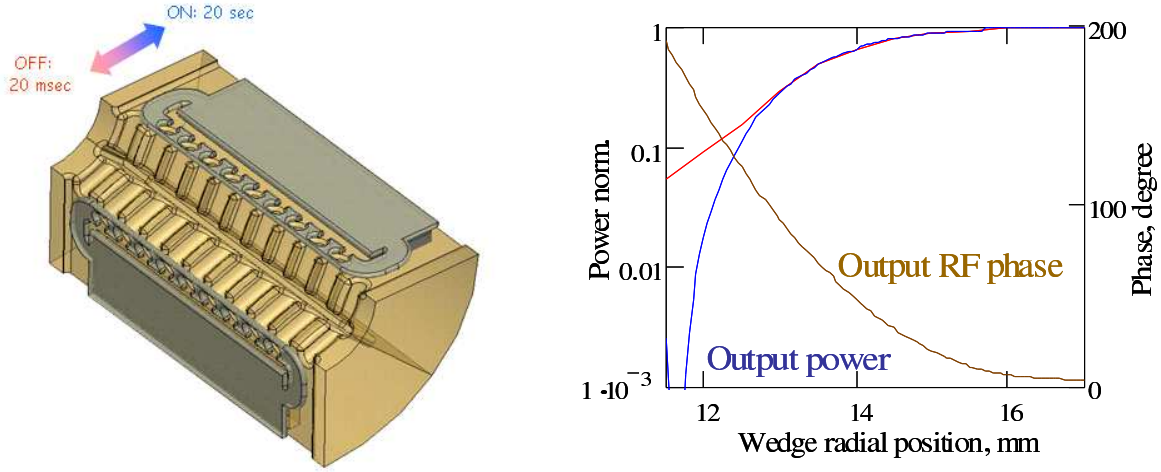

Figure 23: PETS configurations with detuning wedges (left). The produced RF power and RF phase for the different wedge position (right).

the damping slots. This was done using special profiling of the iris, see Fig. 21. Compared to the structure with the circular symmetry, a field enhancement of only 20% was achieved. The maximum surface electric field for the nominal RF power is 48 MV/m.

During machine operation, it will be necessary to locally turn the RF power production OFF when either PETS or an accelerating structure fails due to breakdown. The net RF power generated by the beam at the end of the constant impedance structure will be zero if the structure synchronous frequency is detuned by amount $\pm 2\beta c/(1-\beta)L$, where $\beta - V_g/c$ and L - length of the structure, see [37] for more details. We have found that such a strong detuning can be achieved by inserting four thin wedges through four of the eight damping slots, see Fig. 23. The wedge geometry and the final wedge position are optimised in such a way that at any intermediate wedge position, there is no electrical field enhancement in the gap between the wedge and the wall; thus, the device can operate as a variable attenuator. The produced RF power and RF phase are shown in Fig. 23 for the different wedge position.

In the case of a structure with a high group velocity ($\beta = V_g/c$) and finite length (L), the expression for the wake potential [38] should be evaluated:

$$\begin{aligned} W(z) &= 2q \times K \sin\left(\tfrac{\omega z}{c}\right) e^{-\frac{\omega z}{2Q(1-\beta)c}} \times \left\{1 - \tfrac{\beta z}{L(1-\beta)}\right\} \\ W(z) &= 0, \quad z > L\tfrac{1-\beta}{\beta} \end{aligned} \tag{3}$$

here we have included the catch-up parameter for damping and drain out from the structure of the finite length. Following (3), the best scenario to provide the fast decay of the wakefields is to reduce the Q-factor and to increase the group velocity as much as possible.

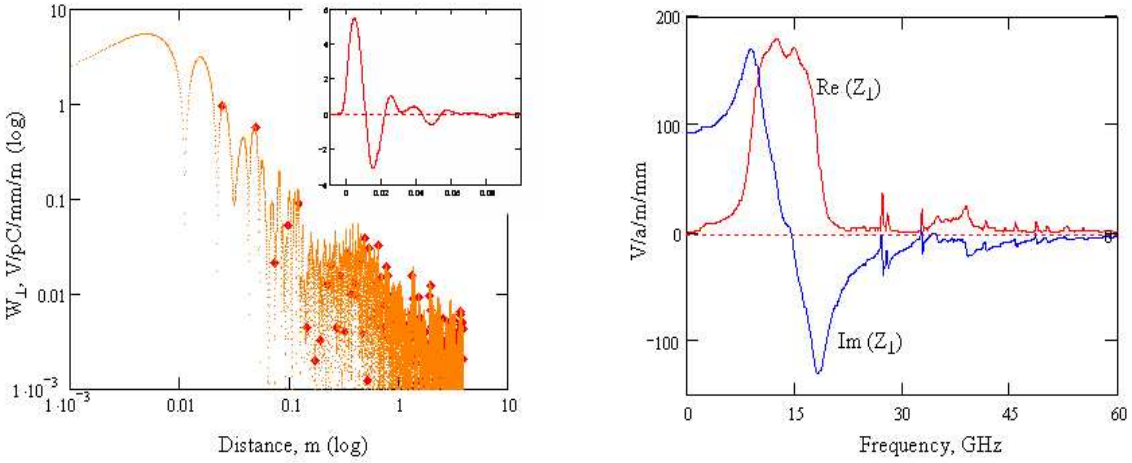

Figure 24: The transverse wake potential (left plot) and impedance (right plot) simulated with GDFIDL for the complete PETS geometry.

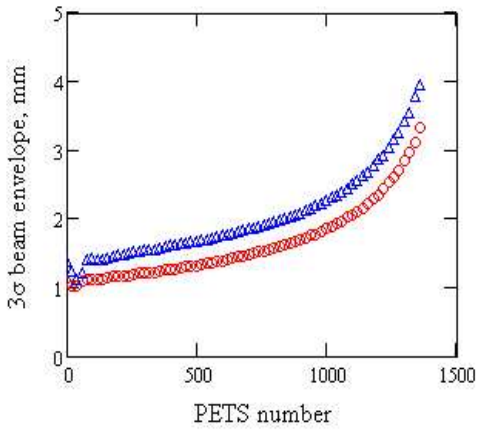

Figure 25: Evolution of the 3σ beam envelope along the decelerator sector; circles – without wakefields, triangles – with wakefields included.

In the presence of the longitudinal slots, the transverse mode field pattern is dramatically distorted so that a considerable amount of the energy is now stored in the slots. The new, TEM-like nature of the mode significantly increases the group velocity, in our case from $0.42c$ to almost $0.7c$. With introduction of the lossy dielectric material close to the slot opening, the situation improves further. The proper choice of the load configuration with respect to the material properties makes it possible to couple the slot mode to a number of the heavily loaded modes in dielectric. This gives a tool to construct the broad wakefields impedance. The transverse wakepotential simulations in a complete PETS geometry were done with GDFIDL [39], see Fig. 24. The computer code PLACET [40] was then used to analyze the beam dynamic along the decelerator in the presence of strong deceleration and calculated wakefields. The results of the simulation (see Fig. 25) clearly indicate that the suppression of the transverse wakefields obtained, is strong enough to guarantee the beam transportation without losses.

8 Drive Beam Generation and Decelerator

The CLIC study focuses on high-gradient, high-frequency (12 GHz) acceleration for multi-TeV linear colliders. Short RF pulses of high peak power are typically required. As a result of the present optimization of the accelerating structure (see section 3), 240 ns long pulses at about 64 MW per accelerating structure are needed for CLIC.

To produce these pulses, the CLIC concept is based on the use of the two-beam acceleration technique [41], in which an electron beam (the drive beam) is accelerated using standard, low-frequency RF sources and then used to produce RF power at high frequency. When using conventional RF sources (klystrons), pulse compression or delayed distribution techniques would be mandatory in order to obtain the needed high peak power and short pulse length. Similar techniques can be used in two-beam accelerators. In such a case, however, the compression and

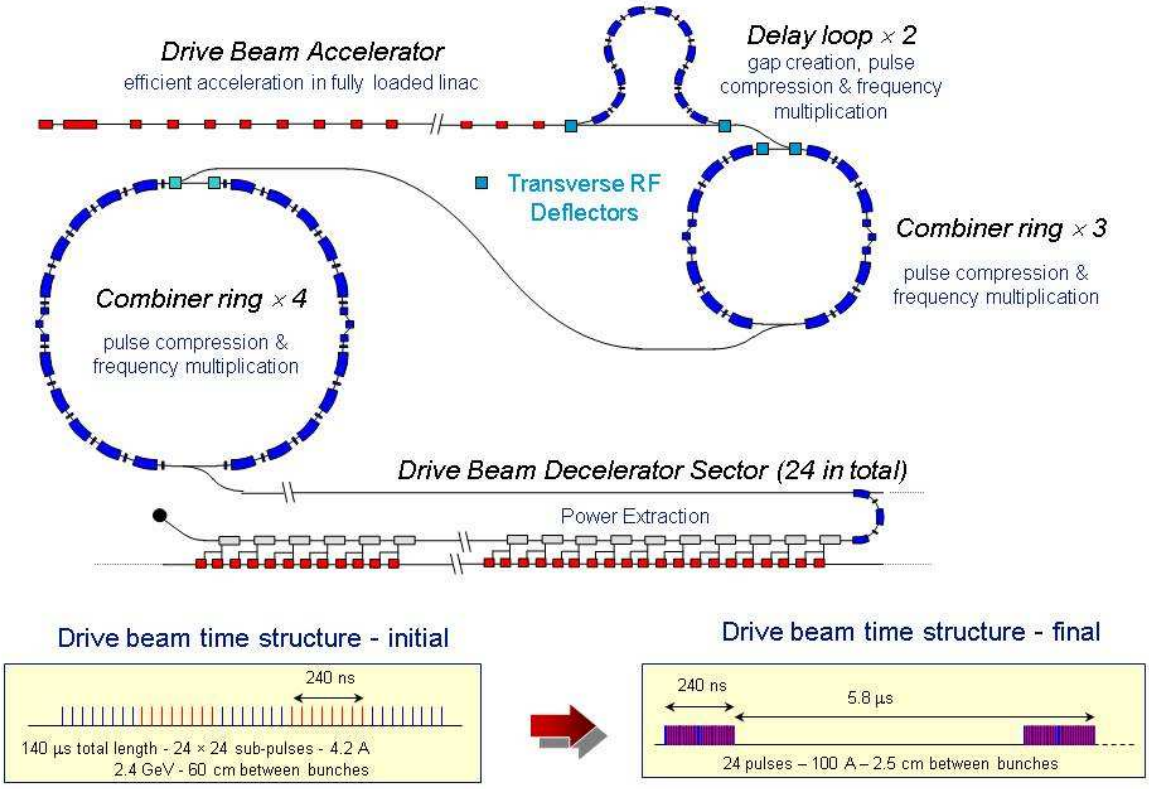

Figure 26: Schematic layout of one CLIC RF power source complex.

distribution are done with electron beams [42]. The main advantage of electron beam manipulation, with respect to manipulation of RF pulses, consists in the very low losses that can be obtained while transporting the beam pulses over long distances and compressing them to very high ratios. A further advantage is the possibility of frequency multiplication, achieved by interleaving bunched beams by means of transverse RF deflectors [43]. In the following we will describe the CLIC RF power source complex used to generate all the RF power needed for one of the two main linacs (electron or positron). A schematic layout of one complex is shown in Figure 26.

The CLIC RF power source can be thought of as a 'black box' that combines and transforms several long, low-frequency RF pulses into many short, high-power pulses at high frequency. During the process, the energy is stored in a relativistic electron beam, which is manipulated in order to obtain the desired time structure and then transported to the place where the energy is needed. The energy is finally extracted from the electron beam in resonant decelerating structures, which run parallel to the main accelerator and are called Power Extraction and Transfer Structures (PETS). The key points of the system are an efficient acceleration of the drive beam in conventional structures, the introduction of transverse RF deflectors to manipulate the drive beam, and the use of several drive-beam pulses in a counter-flow distribution system, each one powering a different section of the main linac. The primary characteristic of this scheme consists of using the energy stored in different time bins of a long electron-beam pulse to create the RF necessary for different sections of a long linac. Thus, the same accelerator and beam manipulation system is used to create all the beam pulses needed for powering one of the two main linacs. The method discussed here seems relatively inexpensive, efficient and very flexible.

The drive-beam generation complex is located at the centre of the linear collider complex, near the final-focus system. The energy for the RF production is initially stored in a 140 μs long electron beam pulse (corresponding to twice the length of the high-gradient main linac) which is accelerated to about 2.4 GeV by a normal-conducting, low-frequency (999.5 MHz) travelling wave linac. The linac is powered by conventional long-pulse klystrons. A high energy transfer efficiency is paramount in this stage. The drive beam is accelerated in relatively short structures, such that the RF losses in the copper are minimized. Furthermore, the structures are fully beam-loaded, i.e. the accelerating gradient is zero at the downstream end of each structure and no RF power flows out to a load. In this way, about 98% of the RF energy can be transferred to the beam [44]. The beam pulse is composed

of 24 $\times$ 24 sub-pulses, each one 240 ns long. In each sub-pulse the electron bunches occupy alternately only the even or odd number buckets of the drive-beam accelerator fundamental frequency (999.5 MHz). Such a time structure can be produced after a thermionic gun in a subharmonic buncher, whose phase is rapidly switched by 180° every 240 ns, as demonstrated in CTF3 [45]. Alternatively, the phase switch can be obtained by manipulation of the laser pulse timing if using a photocathode gun [46]. This provides us with a mean to separate the sub-pulses after acceleration, while keeping a constant current in the accelerator and avoiding transient beam-loading. With nominal phase-switching times, the resulting pulse of the acceleration voltage is rectangular. By delaying the phase-switching time, it is also possible to obtain sub-pulses of different lengths. When the different sub-pulses are superimposed at the end of the combination process, one can thus obtain a current ramp of about 85 ns at the leading edge of the pulse. This in turn produces a ramp in the PETS power output, which is used for beam-loading compensation in the main linac.

As the long pulse leaves the drive-beam accelerator, it passes through a delay-line combiner [42] where odd and even sub-pulses are separated by a transverse RF deflector at the frequency of 499.8 MHz. Each even bunch train is delayed with respect to the following odd one by 240 ns. The sub-pulses are recombined two-by-two by interleaving the electron bunches in a second RF deflector at the same frequency. The net effect is to convert the long pulse to a periodic sequence of drive-beam pulses with gaps in between. After recombination, the pulse is composed of 12 $\times$ 24 sub-pulses (or trains) whose spacing is equal to the train length. The peak power and the bunch frequency are doubled. The same principle of electron-bunch pulse combination is then used to combine the trains three-by-three in a first combiner ring, 145 m long. Two 999.5 MHz RF deflectors create a time-dependent local deformation of the equilibrium orbit in the ring. This bump is used for injection of a first train in the ring (all its bunches being deflected by the second RF deflector onto the equilibrium orbit). The ring length is equal to the spacing between trains plus $\lambda/3$, where λ is the spacing between bunches, equal to the wavelength of the RF deflectors. Thus, for each revolution period, the RF phase seen by the bunches circulating in the ring increases by 120°, and when the second train is injected, the first one is deflected away from the septum and its bunches are interleaved with the ones which are injected (at a $\lambda/3$ distance). This is repeated again, then the three interleaved trains are extracted from the ring by an ejection kicker half a turn later, and the same cycle starts again. After the first combiner ring the whole pulse is composed of 4 $\times$ 24 trains. The trains are combined again by a factor 4, using an analogous mechanism in a second combiner ring 434 m long, and obtaining the final 24 trains required for the main linac. At this point, each final train is 72.4 m long and consists of 2904 bunches with a charge of 8.4 nC/bunch and an energy of 2.4 GeV. Such drive-beam pulses are distributed down the main linac via a common transport line, in a direction opposite to the direction of the main beam. The distance between trains is now 1736 m, corresponding to twice the length of the linac section which they will power, so that they will arrive at the appropriate time to accelerate a high energy beam travelling in the opposite direction. Pulsed magnets deflect each beam at the appropriate time into a turn-around. After the turn-around each pulse is decelerated in a 868 m long sequence of low-impedance Power Extraction and Transfer Structures (PETS) down to a minimum energy close to 0.24 GeV, and the resulting output power is transferred to accelerate the high-energy beam in the main linac. As the main beam travels along, a new drive-beam train periodically joins it and runs in parallel but ahead of it to produce the necessary power for a 868 m long linac unit. At the end of a unit the remaining energy in the drive beam is dumped while a new one takes over the job of accelerating the main beam. The main characteristics of the drive beam complex are given in Tables 6 and 7.

8.1 Accelerator Structures, Design, HOM damping

To accelerate the drive beam, each of the two CLIC drive beam accelerators (DBA) will consist of 326 accelerating structures, each of 33 regular cells and approximately 3.75 m length. With an input power of 33 MW, such a structure would be fully (99.96%) beam loaded with the nominal 4.21 A beam current. The full beam loading would bring the unloaded acceleration of 14.75 MV in a 3.3 m long structure to a loaded moderate 7.63 MV. The calculated RF-to-beam efficiency is 97.3% in this case. Assuming a reduction factor for this efficiency of 96%, thus allowing for a margin for *i)* off-crest acceleration, *ii)* finite bunch length and *iii)* overhead for feedback loop dynamics results in an overall RF-to-beam efficiency of 93% and a reduced acceleration per structure of 7.3 MV, thus the requirement of 326 accelerating structures to achieve the drive beam energy of 2.38 GeV.

Two types of structures have been studied [47]: the "Tapered Damped Structure" (TDS), originally designed for the CLIC main accelerator and downscaled by a factor 30. Dipole mode damping in TDS is attained by coupling wideband SiC loads through four waveguides to the accelerating cavities. The cut-off frequency of these waveguides is chosen above the operating frequency, but below the higher order mode frequencies. It thus serves as a high-pass filter between the cavity and the dampers. A TDS scaled to 999.5 MHz would however be very large (outer diameter 1.3 m).

The impractical size of TDS was one of the reasons to study in detail a novel type of structure [48]. The SICA structure (for "Slotted Iris – Constant Aperture") has four radial slots in each iris, which virtually do not perturb the

Parameter	Symbol	Value	Unit
Nominal gradient	G	100	MV/m
BNS factor	η_{BNS}	0.91	-
HDS filling factor in ML	η_{fill}	0.786	-
HDS length	l_{HDS}	0.2464	m
HDS effective length	l_{HDSeff}	0.229	m
HDS per PETS	n_{hp}	2	-
HDS per Quad	n_{hq}	4	-
HDS peak power	P_{HDS}	63.9	MW
PETS cell unit length	$L_{\mathrm{pets-u}}$	6.25	mm
Nb of cells	n_{pul}	34	-
PETS active length	$L_{\mathrm{p,a}} = L_{\mathrm{pets-u}} n_{\mathrm{pul}}$	0.2126	m
Unit length	$L_{\mathrm{u}} = n_{\mathrm{hq}} l_{\mathrm{HDS}}$	0.9856	m
PETS impedance	$R_{/\mathrm{Q,p}}$	2294.67	Ohm/m
PETS group-velocity /c	$v_{\mathrm{g,p}}$	0.4529	-
DB form factor	F_{DB}	0.9689	-
PETS extraction efficiency	y_{pex}	0.96	-
PETS transfer efficiency	y_{pte}	0.977	-
PETS peak power	$P_{\mathrm{p}} = \frac{P_{\mathrm{HDS}} n_{\mathrm{hp}} a_{\mathrm{Gtune}}^2}{y_{\mathrm{pex}} y_{\mathrm{pte}}}$	136.26	MW
Damping loss factor	η_{damp}	0.9947	-
Drive beam current	$I_{\mathrm{DB}} = \frac{1}{\eta_{\mathrm{damp}}} \sqrt{\frac{4 v_{\mathrm{g,p}} c P_{\mathrm{p}}}{{L_{\mathrm{p,a}}}^2 {F_{\mathrm{DB}}}^2 R_{/\mathrm{Q,p}} 2\pi f_0}}$	100.95	A
HDS per ML	$n_{\mathrm{hds}} = (E_{\mathrm{f}} - E_{\mathrm{in}})/(\eta_{\mathrm{BNS}} l_{\mathrm{HDSeff}} G)$	71568	-
Number of DB stations	N_{sta}	24	-
Linac length	$L_{\mathrm{ML}} = \frac{E_{\mathrm{f}} - E_{\mathrm{in}}}{\eta_{\mathrm{BNS}} \eta_{\mathrm{fill}} G} + 8 N_{\mathrm{sta}}$	21.038	km
HDS per station	$n_{\mathrm{h/s}} = n_{\mathrm{hds}}/N_{\mathrm{sta}}$	2982	-
PETS per station	$n_{\mathrm{p/s}} = n_{\mathrm{h/s}}/n_{\mathrm{hp}}$	1491	-
Station length	$L_{\mathrm{sta}} = L_{\mathrm{ML}}/N_{\mathrm{sta}}$	876.565	m
Residual energy factor	S	0.900	-
Non-gaussian factor	η_{dist}	0.973	-
Overall energy factor	$\eta_{\mathrm{EDB}} = S F_{\mathrm{DB}} \eta_{\mathrm{dist}}$	0.84847	-
DB electron energy	$E_{\mathrm{DB}} = n_{\mathrm{p/s}} P_{\mathrm{p}}/(\eta_{\mathrm{EDB}} I_{\mathrm{DB}})$	2.371	GeV

Table 6: Drive Beam Decelerator parameters.

Parameter	Symbol	Value	Unit
Transit time in Main Linac	$T_{\mathrm{ML}} = L_{\mathrm{ML}}/c$	70.174	μs
Transit time in station	$\tau_{\mathrm{sta}} = L_{\mathrm{sta}}/c$	2.924	μs
DB fill+rise time	$\tau_{\mathrm{f+r}}$	83.4	ns
stacking factor CR1	S_{CR1}	3	-
stacking factor CR2	S_{CR2}	4	-
Folding number	$N_{\mathrm{fold}} = 2 S_{\mathrm{CR1}} S_{\mathrm{CR2}}$	24	-
DB flat pulse duration	$\tau_{\mathrm{flat}} = 2\tau_{\mathrm{sta}}/N_{\mathrm{fold}} - \tau_{\mathrm{f+r}}$	160.26	ns
Train duration	$\tau_{\mathrm{DB2}} = \tau_{\mathrm{f+r}} + \tau_{\mathrm{flat}}$	243.7	ns
Electrons per train	$N_{\mathrm{t}} = \tau_{\mathrm{DB2}} I_{\mathrm{DB}}/q_e$	1.535	10^{14}
Bunches per train	$k_{\mathrm{t2}} = f_0 \tau_{\mathrm{DB2}}$	2922	-
DB bunch population	$n_{\mathrm{DBb}} = I_{\mathrm{DB}}/q_e/f_0$	5.253	10^{10}
DB bunch charge	$Q_{\mathrm{DBb}} = n_{\mathrm{DBb}} q_e$	8.417	nC
Energy of DB train	$E_{\mathrm{t}} = N_{\mathrm{t}} E_{\mathrm{DB}} q_e$	58.33	kJ
Repetition frequency	f_{rep}	50	Hz
Total DB power, 1 beam	$P_{\mathrm{DB,tot}} = f_{\mathrm{rep}} N_{\mathrm{sta}} E_{\mathrm{t}}$	69.99	MW
Delay loop length	$L_{\mathrm{DL}} = \tau_{\mathrm{DB2}} c$	73.047	m
Combiner ring 1 length	$L_{\mathrm{CR1}} = 2 L_{\mathrm{DL}}$	146.094	m
Combiner ring 2 length	$L_{\mathrm{CR2}} = 2 S_{\mathrm{CR1}} L_{\mathrm{DL}}$	438.283	m
Total DB pulse duration	$\tau_{\mathrm{DB,tot}} = 2 N_{\mathrm{sta}} \tau_{\mathrm{sta}}$	140.3	μs

Table 7: Drive beam parameters.

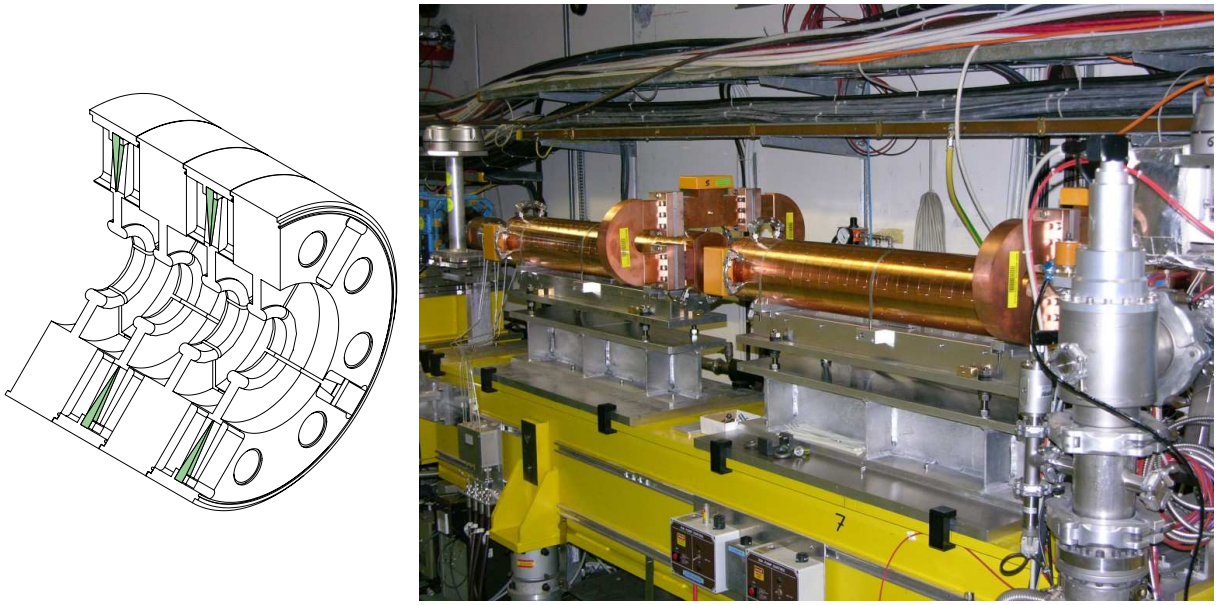

Figure 27: Conceptual view of the accelerating structure (left) and two 3 GHz SICA structures during installation in CTF3 (right).

fundamental mode field; dipole mode currents however are intercepted by the slots. The slots continue radially into ridged waveguides which contain tapered SiC loads. These are designed as to drastically reduce the Q of the dipole modes (to values typically below 20). As opposed to TDS, where the higher order modes are separated by a filter from the accelerating mode, mode separation in SICA uses the geometric differences and special symmetries of the mode patterns. SICA structures were successfully built and tested at 3 GHz and have been implemented as DBA structures for CTF3. At 999.5 MHz, SICA structures would have an outer diameter of approximately 520 mm.

Fig. 27 shows an artists conception of the accelerating structure and a photograph of two 3 GHz SICA structures during installation in CTF3.

Another feature of the SICA structures is the constant iris aperture over the whole length of the accelerating structure which reduces the short range wakes. The detuning is obtained by introducing nose cones with varying depths. These nose cones lead to a larger ratio of surface field to accelerating gradient in the downstream cells (ratio of up to 3.4), but this is acceptable since the overall accelerating gradient is moderate.

Potential issues with the SICA structure were identified and addressed in the design phase. These were *i)* the field enhancement at the slot edges and *ii)* the presence of low frequency "slot modes" and their potential impact on the performance. The field enhancement is reduced to acceptable 40% by a modest rounding of the edges (rounding radius of approximately half the slot width). This additional field enhancement will lead to a maximum surface field of 33 MV/m or 1.2 Kilpatrick at the slot edges in the last cell, which is still acceptably small.

The slot modes, which occur at frequencies of about 2/3 of the operating frequency, have the electric field across the slots and are strongly damped ($Q < 6$) if the cut-off frequency of the ridged waveguide is chosen low enough. The kick factor of the slot mode is found to be at an acceptable 5% of that of the lowest dipole mode.

A total of 20 SICA structures operating at 3 GHz have been built by industry [49]. They have been installed in CTF3 in 2003, and the CTF3 drive beam linac has since been operated routinely under full beam-loading condition [50], both at nominal parameters as well as higher gradients, powers and currents. These many years of successful operation demonstrate that all potential issues have been solved.

The parameters of the DBA accelerating structures both at 3 GHz and at 1 GHz are summarized in Table 8.

9 Beam Instrumentation

This paragraph presents an overview of the CLIC requirements in terms of beam diagnostic and the already achieved performance of the devices tested on the CLIC Test Facility 3 or elsewhere. The Main and the Drive beams are treated separately.

9.1 Drive Beam diagnostics

With a high bunch charge and a high bunch repetition frequency, the Drive Beam is unique. Being the RF power source of the collider, it needs to be operated with a very high level of reliability and stability [51, 52] and the

	3 GHz SICA			1 GHz SICA			unit
operating frequency	2998.55			999.52			MHz
beam current	3.5			4.21			A
	1st cell	**mid cell**	**last cell**	**1st cell**	**mid cell**	**last cell**	
cavity diameter	82.95	79.00	74.39	248.85	237	223.17	mm
nose cone size	0.00	2.53	4.66	0.00	7.59	13.98	mm
iris thickness	6.00			19.20			mm
iris diameter	34.00			108.80			mm
phase advance/cell	120 °			120 °			
r'/Q (Linac-Ω)	3143	3292	3165	982	1029	989	Ω/m
group velocity	5.19	3.49	2.36	5.19	3.49	2.36	% c
Q accelerating mode	13860	12771	10950	24794	22845	19588	
f 1st dipole mode	4147	4197	4097	1296	1314	1279	MHz
Q 1st dipole mode	17.5	6.2	5.8	17.5	6.2	5.7	
kick factor 1st dipole	555	668	843	16.95	20.22	5.9	V/pC/m^2
f 2nd dipole mode	4243	4279	4379	1326	1318	1335	MHz
Q 2nd dipole mode	3.4	17.3	24.4	3.4	17.3	23.4	
kick factor 2nd dipole	206	254	197	6.29	8.07	25.0	V/pC/m^2
cell length	33.32			99.96			mm
number of cells	32			33			
structure length	1.22			3.75			m
fill time (τ)	98			311			ns
input power	30			33			MW
accelerating voltage, unloaded	13.3			14.8			MV
accelerating voltage loaded	7.9			7.6			MV
beam loading (κ)	97.4			99.96			%
calculated efficiency	92.5			97.3			%
assumed efficiency (η)	92.5			93			%
number of structures	2+16			2+326			
total energy gain	127			2380			MeV

Table 8: Drive beam accelerator parameters at 3 GHz and at 1 GHz

monitoring of its beam parameters must be performed with a high level of accuracy. Instruments developed on CTF3 can be reused in the Drive Beam complex. Inductive pick-ups [53] and Wall Current Monitors [54] provide respectively beam position measurements with a spatial resolution better than 100 μm and intensity measurements with an absolute precision better than 1%. A machine protection system of the CTF3 linac has been designed based on the measurement and the comparison of consecutive WCM signals [55]. Beam imaging using Optical Transition Radiators (OTR) are considered as a standard technique to provide emittance and energy spread measurements. Recent studies have been performed to improve performances by optimizing the OTR screen surface, shape and material [56, 57].

Time resolved spectrometry The Drive Beam has been designed for the highest efficiency minimizing electricity consumption. In this context, the drive beam linac accelerating structures are operated in fully beam-loaded condition, meaning that nearly all the RF power, except for ohmic losses, is transferred into beam energy. In this mode of operation, the RF-to-beam transfer efficiency has been measured at 96% [44]. The resulting energy spectrum shows a strong time dependency with higher energies in the first 10-50 nanoseconds of the pulse. Time-resolved spectrometry is therefore an essential beam diagnostic to correctly tune the phase of the accelerating structures. Several methods, based either on the use of segmented dumps [58] or multi-anode photomultiplier tubes [59] have been developed on CTF3. Their design has been studied to be very radiation hard and they have shown time resolution better than 1 ns.

Longitudinal Beam Diagnostic The Drive Beam generation relies on a flexible bunch multiplication frequency technique. To provide the highest efficiency, the performance of the bunch frequency multiplication must be controlled precisely at the picosecond level. Streak cameras combined with Optical Transition Radiation (OTR) or Synchrotron Radiation (SR) have been used for decades for longitudinal profile measurements. With resolution of

few ps [60], they will measure the bunch train combination as it is the case on CTF3 [61]. In addition to the streak camera, a simple, cost effective non-intercepting beam phase monitor [62] has been developed on CTF3 and has already demonstrated its ability to measure the bunch train combination [63].
In the CLIC Drive Beam, the bunch length needs to be controlled precisely [64]. In the linac the bunches must remain short to keep the energy spread as low as possible, but need to be stretched before the rings to minimize emittance dilution due to coherent synchrotron radiation. In addition to the streak camera, other techniques to measure short bunch lengths have been developed. One of the most promising alternative techniques is based on the use of RF deflecting cavities. As the bunch is passing through the cavity, it experiences a time dependent deflection which converts time into spatial information. By measuring the beam size at a downstream location, the longitudinal profile can be extracted. The time resolution depends on the deflecting power, the beam optics at the location of both the deflector and the beam profile monitor, and finally on the spatial resolution of this monitor. With this method time resolution of 10 fs has already been obtained [65]. The Drive Beam RF deflectors used for injection into the rings can also serve for the bunch length measurements. In addition, non-intercepting bunch length monitors have been developed, in particular through the use of an RF pick-up. The device measures and analyzes the power spectrum of the electromagnetic field emitted by the electrons and picked-up by a single waveguide. It is capable of providing single shot non-intercepting bunch length measurements with a resolution better than 300 fs [66] which would be precise enough to cover the Drive Beam requirements.
Considering the very high beam charge of 587 μC in the Drive Beam linac, the use of any intercepting devices like screens or wire scanners cannot be foreseen. So far no alternatives have been found to provide adequate non-intercepting beam size monitors. Laser wire scanners are not well adapted for millimeter beam sizes and low energy beams [67]. Ionization profile monitors or rest gas monitors do not have a good enough spatial resolution [68, 69] and might be disturbed by wakefields. In this context the beam emittance would have to be measured with a reduced beam charge (1/50) by shortening the pulse duration and by lowering the repetition rate of the machine down to 1 Hz. The beam diagnostic of the Drive Beam decelerator has not been investigated yet. With a very high energy spread, new techniques must be envisaged in order to qualify the transverse properties of the beam.

9.2 Main Beam diagnostics

The Main Beam presents unprecedented beam parameters, with beam energy up to 1.5 TeV and extremely small beam emittance and size. The successful operation of the linac is based on an optimization procedure [22, 70, 71] to guarantee the best possible beam alignment and a small emittance growth. Sub-nanometer stabilization [72] is also required in the final focus system to provide the highest luminosity.

Nanometer Beam Position Monitor The beam position has to be controlled very precisely to minimize emittance growth along the main linac. Beam dynamic simulations have shown that to guarantee the performance of the collider, beam position measurements must be performed with an absolute precision of 10 μm and a resolution of 100 nm. One approach, which has already demonstrated good performances [73, 74, 75], is to develop cavity BPMs. Another alternative pursued at CERN is to scale down the inductive pick-up already developed for the CTF3 linac [51]. The achieved resolution obtained so far and scaled to the CLIC beam parameters is 200 nm [76]. Precise Beam Position monitors are developed as well for an energy spectrometer [74] in the Beam Delivery System.

Measuring Small Beam Sizes Emittance measurements are based on transverse beam profile monitors. For micron-beam spot size [77], only one alternative exists and is based on the use of Laser Wires Scanners [67]. A lot of experimental studies have been performed during the last 10 years at DESY [78], KEK [79] and SLAC [80].

Measuring Short Bunch Length In the CLIC Main linac, the bunch length is reduced down to 135 fs. As it was mentioned previously, even if RF Deflecting cavities can provide such fast resolution [81], non-intercepting techniques should be envisaged. A potential solution could be based on the use of Coherent Diffraction Radiation as described in [82].
The luminosity of the collider could be monitored using high energy Beamstrahlung photons from the interaction point [83]. The beam polarization would be measured in the Beam Delivery System presumably using Compton back-scattering.

9.3 Diagnostics for both Beams

Beam Halo Monitors For future linear colliders, it must be ensured that particle losses are minimized, as activation of the vacuum chambers or other components makes maintenance and upgrade work time-consuming and costly. It is imperative to have a clear understanding of the mechanisms that can lead to halo formation and to

Parameter	Requirements		Devices		
	From	Parameters	Method	Performances	Ref
Drive Beam					
Position	Decelerator	Precision $\sim$10mm Resolution $\sim$1mm	Inductive pick-up Re-entrant Cavity	Resolution $\sim$ 200nm (lab) Resolution $\sim$ 3.2mm (lab)	[76] [73]
Energy	Turn-around	Resolution $\sim$ 10-5	Precision BPM	See position monitor	[74]
Bunch Length	Decelerator	Resolution $\sim$ 0.5ps	Streak camera RF Deflector RF pick-up	$>$ 0.2ps better than 0.5ps $>$ 0.5ps	[60] [64] [66]
Phase Stability	Turn-around	0.1°@12 GHz	RF methods	0.1°@12 GHz (electronic)	[90]
Main Beam					
Position	Main Linac	Precision $\sim$ 1mm Resolution $\sim$ 100nm	Inductive pick-up Cavity BPM	Resolution $\sim$180nm (lab) Resolution $\sim$ 15nm (beams)	[76] [75]
Emittance / Size	BDS	Resolution $<$ 1mm	Laser Wire Scanner	Resolution $\sim$1mm	[77]
Energy Spread	BDS	DE/E $\sim 3 \cdot 10^{-4}$	Precision BPM	See position monitor	[74]
Bunch Length	Bunch compressor	Resolution $\sim$ 50fs	RF Deflector Coherent Diffraction Radiation	Resolution 15fs Better than 50fs	[81] [82]

Table 9: Beam Diagnostic Requirements for CLIC

have the possibility to test available theoretical models with an adequate experimental set-up. Measurements based on optical transition radiation are a well-established technique for measurements of the transverse beam profile. However, in order to be suitable for halo measurements as well, the dynamic range of the final image acquisition system needs to be high, being able to cover at least five orders of magnitude in intensity changes. In CTF3, high dynamic imaging system has been investigated since 2004. Beam core suppression techniques were tested on CTF3 using a coronagraph [84]. Innovative camera based on charge injection device (CID) technology [85, 86], which potentially can reach dynamic ranges up to 10^6 as well as improved beam core suppression technique using adaptive optics [87] have been investigated since then.

Femtosecond Phase Monitor and Feedback One important aspect of the two beam acceleration scheme is to synchronize precisely the Main Beam with the RF power produced by the Drive Beam. Timing errors lead to energy variations in the main linac and a subsequent reduction of luminosity. A jitter of 15 fs will give a luminosity reduction of around 2% [88]. It is extremely doubtful that the required tolerance could be met without feedback, feedforward or both types of beam-based correction. A possible scheme [89] for CLIC is to measure the arrival time of the Drive and the Main beams in the transfer lines between the injector complex and the main linac. A precision local clock would be required to keep time from the arrival of the reference until the end of the drive beam train, 140 μs later. Precise time measurements of both beams are performed and compared, and depending on the observed difference, a correction on the drive beam would be applied. Corrections could be done using RF structures, either with deflecting cavities or by varying the energy before the final drive beam bunch compressor. The system relies on a precise timing measurement by means of RF phase and amplitude measurements. A resolution better than 10 fs has been already demonstrated [90] on CTF3.

Beam Loss monitors In a more general context, in order to avoid any beam induced damages, the design of the beam lines and more precisely the use of intercepting devices would have to be compatible with the tolerances defined by the machine protection system. The measurement of beam losses would be an important issue, especially in the CLIC Main tunnel, where both beams would propagate synchronously the one close to the other. The monitors would have to disentangle between losses from the Main and the Drive beams.

A summary of what was said previously is given in Table 9.

10 Overall Layout, Efficiency and AC Power Consumption

Combining the different machine components describes in the preceding sections, the overall CLIC layout with the central injectors for drive and main beams is shown in Figure 28. Table 10 summarizes the space requirements along the main tunnel, thus determining the overall tunnel extent. Figure 29 shows the layout of the main tunnel cross section. The overall diameter is 4.5 m.

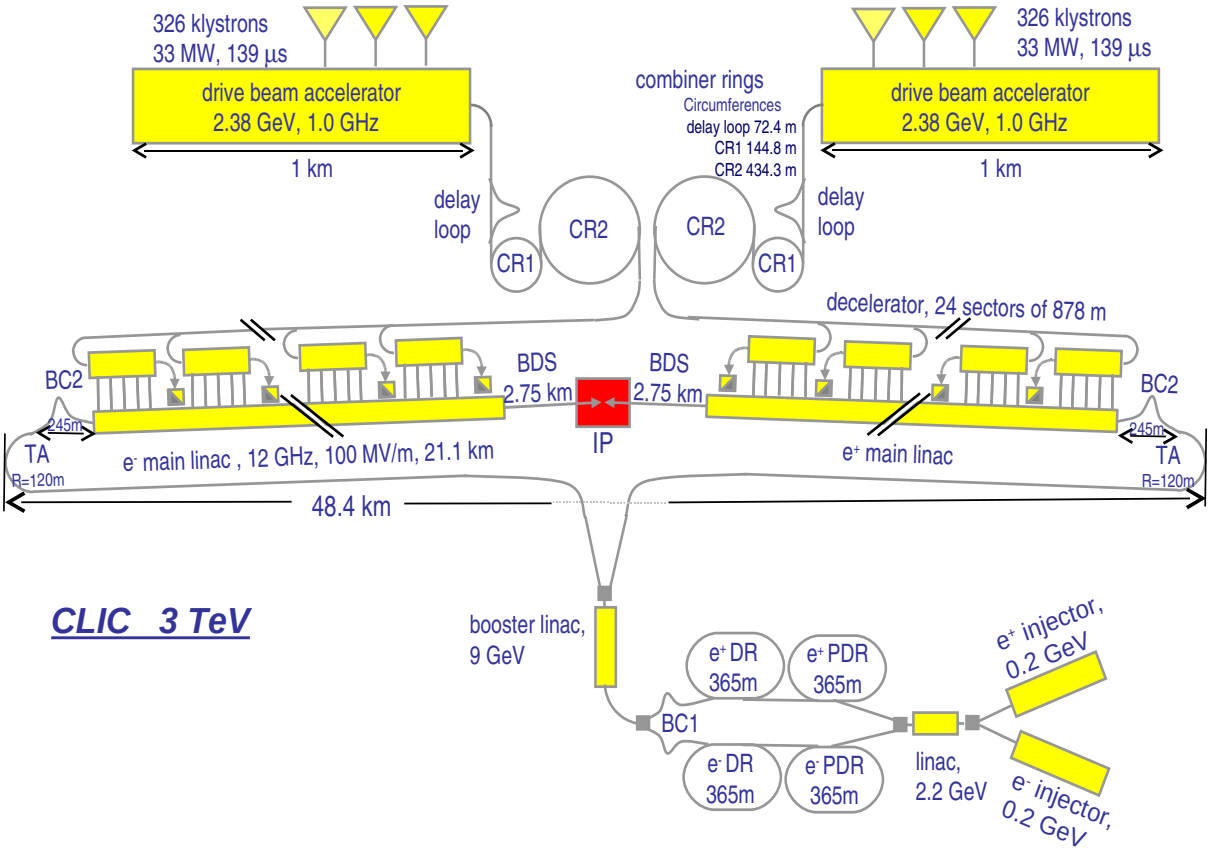

Figure 28: Overall layout of CLIC at 3 TeV

Component	**Length**	**Comments**
R turnaround	120 m	GLC Project report, KEK Report 2003-7, R_{arc}=87 m for 8.25 GeV. $\Delta E \propto E^5/R^3$ gives R=100 m for 9 GeV +20 m margin
Spin Rotator	105 m	ILC spin rotator length EUROTeV-Report-2006-068
BC2 energy correlation cavities	40 m	Assuming 2.3 GV of X band cavities at ∼60 MV/m
Bunch Compressor 2 chicane	40 m	CLIC BC2 design, EUROTeV report 2007-9
Matching and diagnostics	60 m	
Linac-sector × N_{sector}	21077.5 m	24 sectors * 878.23m, with 10% voltage overhead
BDS-diagnostics	370 m	Assuming laser wire with 1 micron resolution able to resolve 20 nm vert. emittance Scales L∝vert emittance x Sqrt(laser resolution)
BDS-collimation	1920 m	Determined by robustness requirement for energy collimator
BDS final focus	460 m	assuming L*=3.5m
Half total length	24192.5 m	
Total	**48385 m**	

Table 10: Space inventory for tunnel length.

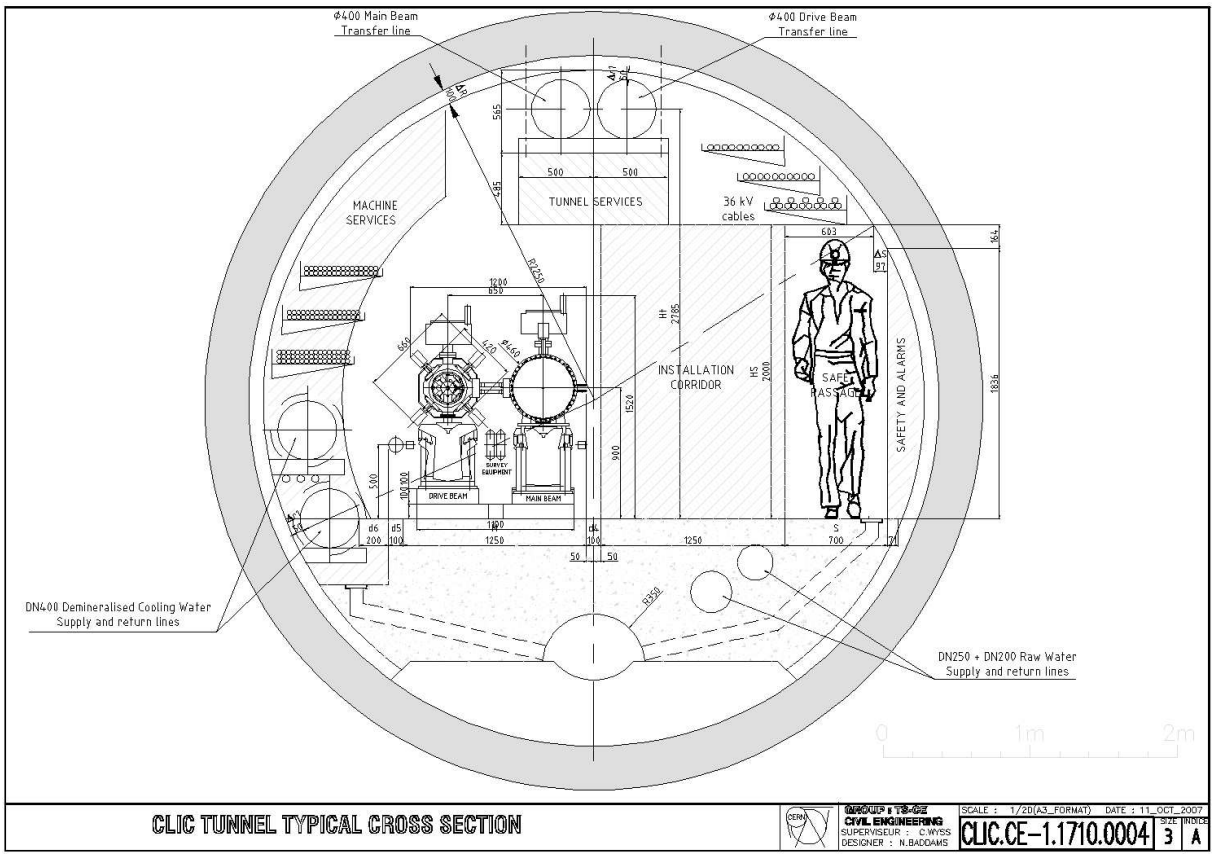

Figure 29: Tunnel cross section

While the main tunnel with the main linacs, decelerators and return lines is deep underground, the injectors are installed in cut and fill tunnels close to the surface. Surface to deep tunnel transfer lines are located between the 9 GeV booster and the main beam return lines, and between the 2nd combiner ring and the drive beam return lines respectively. With two independent drive beam generation complexes the length of the transfer lines between combiner rings and the deep tunnel is no longer constraint by timing issues as it was in the former CLIC design[1]. Table 11 shows the total AC power requirements taking all significant consumers into account. The numbers for magnet power consumption assume standard warm magnet technology. Considering the substantial power consumption of the various beamlines, permanent magnet technology should be considered for some of the beamlines to reduce the overall consumption. For cooling and ventilation power estimates we use the same assumptions as in [91], namely 3% of the dissipated power for water cooling and 40% for ventilation cooling. For instrumentation we assume 100 W per meter of tunnel and for technical infrastructure we assume 50 W per meter of tunnel. For drive beam klystron auxiliaries we estimate 12 kW per klystron. For the detector the same power consumption as for the LHC CMS detector is assumed [92]. Figure 30 illustrates power flow from wall plug to main beam and related efficiencies.

Main beam magnets	Grid power [MW]
Injector linacs	1.2
Positron pre-damping ring	0.8
Electron pre-damping ring	0.3
Damping rings warm magnets	2.2
Damping ring SC wigglers	0.5
Surface to tunnel transfer	2.1
Return lines	1.0
Turn arounds	2.2
Main linacs	8.4
Beam delivery system	3.0
Spent beam lines	4.1
Main beam magnets total	**25.8**
Main Beam Injector RF	
Positron production linac	0.5
Main beam linacs 2.4 and 9 GeV	1.8
Pre-damping rings	6.5
Damping rings	6.5
Main beam injector RF total	**15.2**

Drive beam magnets	Grid power [MW]
DB Accelerator	0.4
Delay loops	1.2
Combiner rings 1	1.3
Combiner rings 2	1.3
Surface to tunnel transfer	1.3
Return lines	0.3
Turn arounds	32.7
Decelerators	7.7
Beam dumps	0.5
Drive beam magnets total	**46.7**
Drive beam linac RF	
Modulator auxiliaries	7.8
RF power	255.5
Drive beam linac RF total	**263.3**
Beam, RF and alignment instrumentation	**5.0**
Detector	**15.0**
Water systems	**9.8**
Ventilation systems	**8.8**
Tunnel infrastructure	**2.5**
Grand total	**392.1**

Table 11: CLIC 3 TeV power consumption

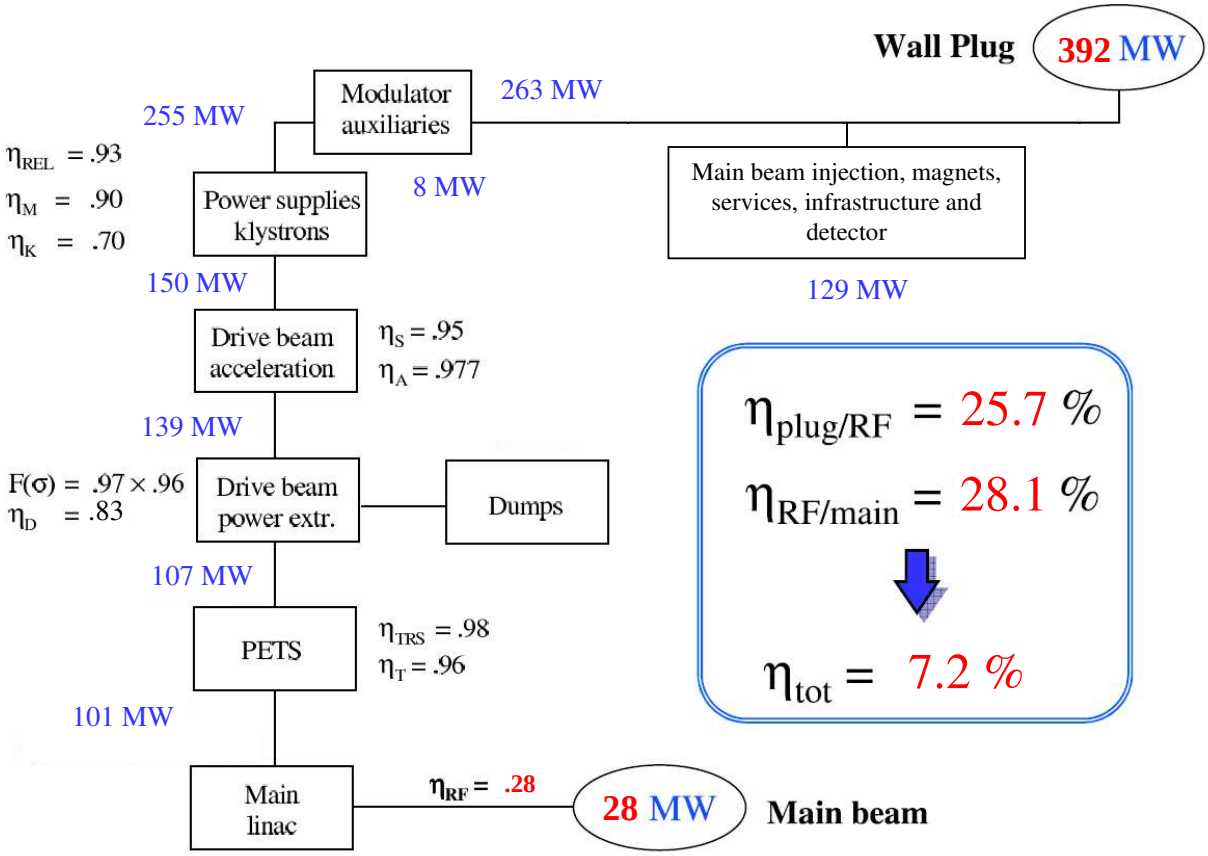

Figure 30: Power flow diagram with component efficiencies

Appendix

A Tables of Parameters

Parameter	*Symbol*	Value	*Unit*
Overall Parameters			
Centre of mass energy	E_{CMS}	3000	GeV
Main Linac RF Frequency	f_{rf}	11.994	GHz
Luminosity	L	5.9	$10^{34}\mathrm{cm}^{-2}\mathrm{s}^{-1}$
Luminosity (in 1% of energy)	$\mathrm{L}_{99\%}$	2	$10^{34}\mathrm{cm}^{-2}\mathrm{s}^{-1}$
Linac repetition rate	f_{rep}	50	Hz
No. of particles / bunch	N	3.72	10^9
No. of bunches / pulse	N_b	312	
Bunch separation	$\Delta \mathrm{t}_b$	0.5 (6 periods)	ns
Bunch train length	τ_{train}	156	ns
Beam power / beam	P_b	14	MW
Unloaded / loaded gradient	$G_{\mathrm{unl/l}}$	120 / 100	MV/m
Overall two linac length	l_{linac}	42.16	km
Total beam delivery length	l_{BD}	2 x 2.75	km
Proposed site length	l_{tot}	48.4	km
Total site AC power	P_{tot}	392	MW
Wall plug to main beam power efficiency	η_{tot}	7.1	%

Table 12: Overall parameters

Parameter	*Symbol*	Value	*Unit*
Main Linac			
Fill factor	F	78.6	%
Overhead for energy fdbk & repair	$\mathrm{ovh}_{\mathrm{rep}}$	5	%
Overhead for off-crest operation	$\mathrm{ovh}_{\mathrm{off\text{-}crest}}$	5	%
Acceleration structure length (active)	l_{struct}	0.229	m
average $\langle a/\lambda \rangle$	a/λ	0.11	
Group velocity	v_g/c	1.66 - 0.83	%
Filling time / rise time	τ_f,τ_r	62.9 / 22.4	ns
Unloaded Quality factor	Q	6100 - 6265	
Shunt impedance (first/last cell)	r_s	89 / 112	(Linac)MΩ/m
RF -> main beam efficiency	$\eta_{b,\mathrm{RF}}$	27.7	%

Table 13: Main linac and accelerating structure parameters

Parameter	*Symbol*	Value	*Unit*
Main Beam in damping ring before extraction			
Energy	$E_{b,\mathrm{DR}}$	2.424	GeV
No. of particles / bunch	N_b	3.72+10%	10^9
Bunch length	$\sigma_{s,\mathrm{DR}}$	1.53	mm
Energy spread	σ_E/E_{DR}	0.134	%
Transverse horizontal emittance	$\gamma\varepsilon_{x,\mathrm{DR}}$	381	nm rad
Transverse vertical emittance	$\gamma\varepsilon_{y,\mathrm{DR}}$	4.1	nm rad
Longitudinal emittance (normalised)		4996	eVm
Electron / positron damping ring			
Ring circumference	C_{DR}	365.2	m
Number of trains stored	n_{train}	1	
Number of bunches / train	N_b	312	
Bunch separation	$\Delta t_{b,\mathrm{DR}}$	0.5	ns
RF frequency	f_{DR}	2	GHz
Wiggler length	l_{wig}	152	m
Damping times	τ_x / τ_y / τ_z	1.5 / 1.5 / 0.76	ms
Tunes	Q_x/ Q_y	69.84/ 33.80	
Main Beam at linac injection			
Energy	$E_{b,\mathrm{inj}}$	9	GeV
No. of particles / bunch	N_b	3.72	10^9
Bunch length	$\sigma_{s,\mathrm{inj}}$	44	μm
Energy spread	$\Delta E/E_{\mathrm{inj}}$	1.3	%
Transverse horizontal emittance	$\gamma\varepsilon_{x,\mathrm{inj}}$	600	nm rad
Transverse vertical emittance	$\gamma\varepsilon_{y,\mathrm{inj}}$	10	nm rad

Table 14: Main Beam and damping ring parameters

Parameter	*Symbol*	Value	*Unit*
Beam Delivery System + IP			
Total diagnostic section length	l_{coll}	2x 0.37	km
Total collimation system length	l_{coll}	2x 1.92	km
Total final Focus system length	l_{FF}	2x 0.46	km
Input transverse horizontal emittance	ε_x	660	nm rad
Input transverse vertical emittance	ε_y	20	nm rad
Nominal horizontal IP beta function	β_x^*	6.9	mm
Nominal vertical IP beta function	β_y^*	0.068	mm
Horizontal IP core beam size	σ_x^*	45	nm
Vertical IP core beam size	σ_y^*	0.9	nm
Bunch length	$\sigma_{s,\mathrm{inj}}$	44	μm
Initial RMS Energy spread	$\sigma^*_{\Delta E/E}$	0.29	%
Total Energy spread		1	%
Crossing angle at IP	θ_C	20	mrad
Beamstrahlung mom. spread	δ_B	29	%
No. of photons / electron	n_γ	2.2	
No. of coherent pairs / bunch crossing	N_{coh}	38	10^7
No. of incoherent pairs / bunch crossing	N_{incoh}	0.03	10^7
Hadronic events / crossing	N_{hadron}	2.7	
Total luminosity	L_{pk}	6.0	$10^{34}\mathrm{cm}^{-2}\mathrm{s}^{-1}$
Luminosity (in 1% of energy)	$L_{99\%}$	2.0	$10^{34}\mathrm{cm}^{-2}\mathrm{s}^{-1}$

Table 15: Beam Delivery System, IP and background parameters

Parameter	*Symbol*	Value	*Unit*
Decelerator			
No. of drive beam sectors / linac	N_S	24	
Unit length (total)	l_{unit}	876.565	m
Average fill factor	F		%
No. of PETS / sector	$N_{\mathrm{PETS,unit}}$	1491	
Length of PETS (active)	l_{PETS}	0.213	m
Nominal output RF Power / PETS	P_{out}	136	MW
Transfer efficiency PETS $>$ HDS		93.8	%
Number of accelerating structures / PETS		2	
Main beam acceleration power / PETS	P_{acc}	2 x 63.9	MW
Main beam energy gain / unit	ΔE_{main}	62.5	GeV
drive beam -> RF efficiency (HDS input)	η_{decRF}	65	%

Table 16: Decelerator and PETS parameters

Parameter	*Symbol*	Value	*Unit*
Drive beam basic parameters			
Energy (decelerator injection)	$E_{\mathrm{in,dec}}$	2.371	GeV
Energy (final, minimum)	$E_{\mathrm{fin,dec}}$	237	MeV
Average current in pulse	I_{dec}	101	A
Train duration	τ_{train}	243.7	ns
No. bunches / train	$N_{b,\mathrm{dec}}$	2922	
Bunch charge	$Q_{b,\mathrm{dec}}$	8.4	nC
Bunch separation	$\Delta_{b,\mathrm{dec}}$	0.083	ns
Bunch length, rms	$\sigma_{s,\mathrm{dec}}$	1	mm
Normalised emittance, rms	$\gamma\varepsilon_{\mathrm{dec}}$	150	μm rad
Drive Beam linac			
RF frequency	f_{RF}	999.5	MHz
Total number of klystrons	N_{kly}	2 * 326	
Klystron peak power	P_{kly}	33	MW
Repetition frequency	f_{rep}	50	Hz
Beam energy	E_{DB}	2.37	GeV
Pulse length (total train)	τ_{pulse}	140.3	μs
Beam current per pulse	I_{DB}	4.2	A
Charge per pulse	Q_{pulse}	590	μC
Number of bunches / pulse	$N_{b,\mathrm{pulse}}$	70128	
Bunch length (rms)	σ_s	4	mm
Normalised emittance (at injection)	$\gamma\varepsilon_i$	100	μm rad
Total energy spread (at injection)	ΔE/E	1	%
RF -> drive beam efficiency	$\eta_{b,\mathrm{RF}}$	93	%

Table 17: Drive Beam parameters

Parameter	***Symbol***	**Value**	***Unit***
Delay Line			
Length	L_D	73.047	m
RF deflector frequency	f_D	499.8	MHz
Combination factor	$F_{C,D}$	2	
Bunch length (rms)	σ_s	2	mm
Combiner Ring 1			
Length	L_{R1}	146.094	m
RF deflector frequency	f_{R1}	999.5	MHz
Combination factor	$F_{C,R1}$	3	
Bunch length (rms)	σ_s	2	mm
Combiner Ring 2			
Length	L_{R2}	438.283	m
RF deflector frequency	f_{R2}	2998.6	MHz
Combination factor	$F_{C,R2}$	4	
Bunch length (rms)	σ_s	2	mm

Table 18: Delay Line and Combiner Ring parameter

References

[1] F. Tecker *et al.*, "Updated CLIC parameters 2005", CLIC note 627, 2006

[2] M. Battaglia, A. de Roeck, J. Ellis, D. Schulte (editors), "Physics at the CLIC Multi-TeV Linear Collider : report of the CLIC Physics Working Group", CERN report 2004-005, hep-ph/0412251

[3] J.Y. Raguin, I. Wilson, W. Wuensch, "Progress in the Design of a Damped and Tapered Accelerating Structure for CLIC", Proc. PAC 2003 and CLIC Note 567 (2003)

[4] D. Schulte, "Luminosity Limitations at the Multi TeV Linear Collider Energy Frontier," Proc. EPAC 2002 and CLIC Note 527 (2002)

[5] W. Wuensch, H. Braun, S. Doebert, I. Syratchev, and I. Wilson, "A Demonstration of High-Gradient Acceleration", PAC'03, CLIC Note 569 (2003)

[6] S.T. Heikkinen , S. Calatroni, H. Neupert, "Thermal fatigue issues in high gradient particle accelerators", 6^{th} international congress on thermal stresses, 26-29 May, 2005, Vienna, AUSTRIA

[7] W. Wuensch, "Progress in Understanding the High-Gradient Limitations of Accelerating Structures", Advanced Accelerator Concepts: 12th Workshop, Wisconsin, AIP Conf. Proc.: 877 (2006)

[8] H. Braun. Private communication

[9] L. Rinolfi, "The CLIC Main Beam Injector Complex, A review in 2008", CLIC Note 750.

[10] A. Ferrari, A. Latina, L. Rinolfi, "Design Study of the CLIC Injector and Booster Linacs with the 2007 Beam Parameters", CLIC Note 737

[11] M. Poelker, "CLIC workshop 2007", http://indico.cern.ch/conferenceDisplay.py?confId=17870

[12] P. Saez et al., "Polarization studies of strained GaAs photocathodes at the SLAC Gun Test Laboratory", http://citeseer.ist.psu.edu/256582.html

[13] X. Artru et al., Nucl.Instr. and Meth. B 240 (2005) 762

[14] X. Artru et al., Nucl.Instr. and Meth. B 266 (2008) 3868

[15] R. Chehab, POSIPOL 2008, Hiroshima, June 2008, http://home.hiroshima-u.ac.jp/posipol/

[16] M.Korostelev, "Optics design and performance of an ultra-low emittance damping ring for the Compact Linear Collider", EPFL, 2006.

[17] S. Casalbuoni, et al., "Superconductive damping wiglers for the CLIC project", PAC07, Albuquerque, USA.

[18] Y. Papaphilippou, H. Braun and M. Korostelev, "Parameter Scan for the CLIC Damping Rings", EPAC08, Genova, Italy.

[19] W. Bruns, G. Rumolo and Y. Papaphilippou, "Electron cloud build-up and instability in the CLIC Damping Rings", EPAC08, Genova, Italy.

[20] http://www.eurotev.org

[21] F. Stulle, A. Adelmann, M. Pedrozzi, "Conceptual design of bunch compressors and turn around loops for a multi-TeV linear collider", EuroTeV-Report 2008-025

[22] D. Schulte, "Emittance Preservation in the Main Linac of CLIC", EPAC'98, Stockholm, Sweden, CLIC Note 370, CERN/PS/98-018 (LP)

[23] to be published.

[24] R. Tomás, "Optimizing the CLIC Beam Delivery System", CLIC Note 735 (2008)

[25] CLIC lattice repository: http://cern.ch/CLICr

[26] I. Agapov, Private Communication

[27] R. Tomás, CLIC meeting 21 September 2007

[28] S. Fartoukh, J-B. Jeanneret, J. Pancin, "Heat Deposition by Transient Beam Passage in Spoilers", CERN-SL-2001-012 AP and CLIC Note 477 (2001)

[29] R. Tomás, "Non-linear Optimization of Beam Lines", Phys. Rev ST Accel. Beams 0, 081010 (2006)

[30] A. Ferrari, "Impact of the new CLIC beam parameters on the design of the post-collision line and its exit window", CLIC note 739, EUROTeV-Report 2008-021.

[31] V. Ziemann, "CLIC Post-Collision Diagnostics", CLIC note 736, EUROTEV-Report 2008-016

[32] A. Ferrari, V. Ziemann, "Conceptual design of a vacuum window at the exit of the CLIC post-collision line", CLIC note 732, EUROTeV-Report 2008-009

[33] G. Riddone et al., "Technical Specification for the CLIC two-beam module", EPAC08, Genova, Italy

[34] W. Wuensch, "Progress in Understanding the High-Gradient Limitations of Accelerating Structures", CLIC-Note-706 (2007)

[35] I. Syratchev, "Mode Launcher as an Alternative Approach to the Cavity-Based RF Coupler of Periodic Structures", CLIC-Note-503 (2002)

[36] Ansoft Corporation - HFSS. http://www.ansoft.com/

[37] I. Syratchev, "30 GHz High Power Production for CLIC", 7th Workshop on High Energy Density and High Power RF, Kalamata, Greece, 13-17 June 2005

[38] P.B. Wilson, "Introduction to Wakefields and Wake Potentials", SLAC-PUB-4547 (1989)

[39] The GdfidL Electromagnetic Field simulator. http://www.gdfidl.de/
[40] D. Schulte et al., "Simulation Package based on PLACET", Proceedings PAC 2001, Chicago, pp. 3033-3035
[41] A.M. Sessler, "The FEL as a power source for a high gradient accelerating structure", AIP Conf. Proc. 91 (Ed. P.J. Channel), p. 154 (1982).
[42] H.H. Braun et al., "The CLIC RF Power Source. A Novel Scheme of Two-Beam Acceleration for Electron Positron Linear Colliders", CERN 9906 (1999).
[43] R. Corsini and J.-P. Delahaye, "The CLIC multidrive-beam scheme", CERN/PS 98008 (LP) (1998) and CLIC Note 331 (1998).
[44] H.H. Braun, R. Corsini, S. Döbert, E. Jensen, F. Tecker, P. Urschütz, "Efficient long-pulse fully-loaded CTF3 linac operation", Proceedings of 2006 Linear Accelerator Conference, Knoxville, TN, USA, 21 - 25 Aug 2006 and CLIC Note 697.
[45] P. Urschütz, H. H. Braun, G. Carron, R. Corsini, S. Döbert, T. Lefevre, G. McMonagle, J. Mourier, J. Sladen, F. Tecker, L. Thorndahl, C. Welsch, "Beam Dynamics and First Operation of the Sub-Harmonic Bunching System in the CTF3 Injector", Proceedings of EPAC'06, Edinburgh, UK, June 26-30, 2006 and CLIC-Note-683.
[46] R. Losito, G. Bienvenu, H.H. Braun, N. Champault, E. Chevallay, M. Divall, V. Fedosseev, G. Hirst, A. Kumar, G. Kurdi, W. Martin, A. Masi, B. Mercier, I. Musgrave, C. Prevost, I. Ross, R. Roux, E. Springate, G. Suberlucq, "The Phin Photoinjector for the CTF3 Drive Beam", Proceedings of EPAC'06, Edinburgh, UK, June 26-30, 2006 and CLIC-Note-684.
[47] G. Carron, E. Jensen, M. Luong, A. Millich, E. Rugo, I. Syratchev, L. Thorndahl, "Design of a 3 GHz Accelerator Structure for the CLIC Test Facility (CTF3) Drive Beam", Linac 2000, TUA16, CLIC Note 451 (2000)
[48] E. Jensen, I. Syratchev, W. Wuensch, "Slotted-Iris Structure Studies", PAC 2001, MPPH040, CLIC Note 481 (2001)
[49] E. Jensen, "CLIC Drive Beam Accelerating Structures", LINAC 2002, CLIC Note 538 (2002)
[50] R. Corsini et al., "First Full Beam Loading Operation with the CTF3 Linac", EPAC 2004, CLIC Note 604 (2004)
[51] D. Schulte and F. Zimmermann, "Phase and Amplitude Tolerance in the CLIC Main Linac", CLIC Note 588 (2003)
[52] R. Corsini and D. Schulte, "Beam Transverse Stability in the CLIC Combiner Rings", CERN/PS 2002-072 and CLIC Note 539 (2002)
[53] M. Gasior, "A Current Mode Inductive Pick-Up for Beam Position and Current Measurement", Proceeding of DIPAC 2005, Lyon, France, pp.175
[54] P. Odier, "A New Wide Band Wall Current Monitor", Proceeding of DIPAC 2003, Mainz, Germany, pp.216
[55] D. Belohrad, "First Tests of the Machine Protection System for CTF3", Proceeding of DIPAC 2005, Lyon, France, pp.255
[56] C.P. Welsch, E. Bravin and T. Lefèvre, "Optimization of OTR Screen Surface Materials and OTR Screen Geometry at CTF3", Review of Advanced Material Science 16 (2007) 73-79.
[57] C. Welsch, E. Bravin and T. Lefèvre, "Investigations of OTR Screen Surfaces and Shapes", Proceeding of EPAC 2006, Edinburgh, UK, pp.1220
[58] T. Lefèvre et al, "Segmented Beam Dump for Time Resolved Spectrometry on a High Current Electron Beam", Proceeding of DIPAC 2007, Venice, Italy, pp. ; CERN-AB-2007-030-BI
[59] T. Lefèvre et al, "Time Resolved Spectrometry on the CLIC Test Facility 3", Proceeding of EPAC 2006, Edinburgh, UK, pp. 795; CERN-AB-2006-079
[60] Hamamatsu model FESCA 200
[61] C. Welsch et al, "Longitudinal Beam Profile Measurements at CTF3 Using a Streak Camera", Journal of Instrumentation, 1, (2006), P09002
[62] A. Ferrari et al, "Development of a Bunch Frequency Monitor for the Preliminary Phase of the CTF3", Proceeding of DIPAC 2003, Mainz, Germany, pp.211
[63] R. Corsini et al, "Experimental Results on Electron Beam Combination and Bunch Frequency Multiplication", Phys. Rev. STAB 7, 04101, (2004)
[64] A. Ghigo et al, "Commissioning and First Measurements on the CTF3 Chicane", Proceeding of PAC 2005, Knoxville, Tennessee, USA, pp.785
[65] P. Emma et al, "A Transverse RF Deflecting Structure for Bunch Length and Phase Space Diagnostics", LCLS-TN-00-12, (2000)
[66] A. Dabrowski et al, "Non Destructive Single Shot Bunch Length Measurements at CTF3", Proceeding of the PAC 2007, Albuquerque, New Mexico, USA, pp.4069
[67] T. Lefevre,"Laser Wire Scanners, Basic Process and Perspectives for the CTFs and the CLIC Machines", CERN-PS-BD-Note-2001-015, CLIC Note 504.

[68] A. Jansson et al,"Tevatron Ionization Profile Monitoring", European Particle Accelerator Conference, Edinburgh, Scotland, (2006) p.2777
[69] B. Dehning, C. Fischer, J. Koopman and F. Roncarolo,"Accuracy of the SPS Transverse Emittance Monitors", CERN-AB-2005-081
[70] A. Latina, P. Eliasson and D. Schulte, "Bunch compressor for Beam Based Alignment", CERN-AB-2007-035, CLIC Note 713
[71] P. Eliasson and D. Schulte, "Luminosity tuning Bumps in the CLIC Main Linac", CERN-AB-2005-046, CLIC Note 629
[72] S. Redaelli, "Stabilization of Nanometre-Size Particle Beams in the Final Focus System of the Compact LInear Collider (CLIC)", Ph.D. thesis U. Lausanne, CLIC Note 595 (2004)
[73] C. Simon et al, "Installation and calibration of the New Re-entrant BPM in the FLASH linac", Care-Report-06-030
[74] M. Slater et al, "Cavity BPM System Tests for the ILC Energy Spectrometer", Slac-Pub-13031, EuroTeV-2007-059
[75] S. Walston et al, "Performance of a High Resolution Cavity Beam Position Monitor System", Nuclear Instruments and Methods A578 (2007) p.122
[76] I. Podadera and L. Soby, "Precision Beam Position Monitor for EuroTeV", Dipac 07, Venice, Italy, 20-23 May 2006
[77] P. Tenenbaum and Tsumoru Shintake, "Measurements of Small Electron Beam Spots", SLAC-PUB-8057
[78] K. Balewski et al, "Beam Profile Measurements at PETRA with the Laser Wire Compton Scattering Monitor", Proceeding of EPAC 2004, Lucerne, Switzerland, pp. 2526
[79] Y. Honda et al, "Upgraded Laser Wire Beam Profile Monitor", Nuclear Instruments and Methods in Phys. Res. A 538 (2005) 100
[80] R. Alley et al, "A Laser-based Beam Profile monitor for the SLC/SLD Interaction Region", Nuclear Instruments and Methods in Phys. Res. A 379 (1996) 363
[81] M. Huening et al, "Observation of Femtosecond Bunch Length Using a Transverse Deflecting Structure", Free Electron Laser Conference, Stanford, California,(2005) p.538
[82] O. Grimm, "Coherent Radiation Diagnostics for Short Bunches", Particle Accelerator Conference (PAC 07), Albuquerque, New Mexico, (2007) p.2653
[83] P. Eliasson, M. Korostelev, D. Schulte, R. Tomas and F. Zimmermann, "Luminosity Tuning at the Interaction Point", CERN-AB-2006-044, CLIC Note 669.
[84] T. Lefèvre et al, "Beam Halo Monitoring at CTF3", Proceeding of EPAC 2004, Lucerne, Switzerland; CLIC note 610
[85] C.P. Welsch et al, "High dynamic range beam profile measurements", CERN-AB-2006-068; CLIC-Note-686; CTF3-Note-081
[86] C.P. Welsch et al, "Alternative Techniques for Beam Halo Measurements", Measurement Science and Technology 17 (2006) 2035-2040
[87] C.P. Welsch, E. Bravin and T. Lefèvre, "A Beam Halo Monitor Based on Adaptive Optics", Proceeding SPIE Europe Optical Metrology (2007), Munich, Germany
[88] D. Schulte, E. J. N. Wilson and F. Zimmermann, "The Impact of Longitudinal Drive Beam Jitter on the CLIC Luminosity", CLIC Note 598
[89] A. Andersson and J.P.H. Sladen, "Precise Beam Timing Measurement System for CLIC Synchronization", Proceeding of EPAC 2006, Edinburgh, UK, pp. 1211
[90] A. Andersson and J.P.H. Sladen, "RF-based Electron Beam Timing Measurement with sub-10fs Resolution", CERN-AB-2008-003-RF, CLIC note 734
[91] The CLIC Study Team (edited by G. Guignard), "A 3 TeV e+/e- Linear Collider Based on CLIC Technology", CERN Report 2000-008
[92] Lucie Linssen, priv. comm.